

# Loaded Transmission Lines Illuminated Above Ground

Thomas Stuart

Thesis presented in partial fulfilment of the requirements  
for the degree of Master of Science (Engineering) at the  
University of Stellenbosch

Supervisor  
Prof. H. C. Reader

December 1999



## DECLARATION

---

I, the undersigned, hereby declare that the work contained in this thesis is my own original work and that I have not previously in its entirety or in part submitted it at any university for any degree.

Date: 24 September 1999

T. Stuart

# ABSTRACT

---

**Keywords:** MTL, EMI, EMC, measurement

This thesis provides a solution to an EMC problem that arose from an open cast mining system, which suffered from premature detonation. The industry problem is treated as a generic wiring problem, where a transmission line above a ground is illuminated by a plane wave noise source. By choosing appropriate transmission line termination loads, a minimum in the noise power at one termination is sought.

Systematic variation of the loads is carried out above both an ideal and a lossy ground. Simulations are performed using NEC4D, which is a well established wire-based method-of-moments frequency-domain code, and MTL\_SIM, which is a one-dimensional finite-difference time-domain code.

A careful measurement above each type of ground is performed to confirm the accuracy of the measurements. In order to perform a measurement above lossy ground an artificial dielectric with electrical characteristics similar to soil is used. The electrical characteristics of the artificial soil are measured using a stripline system that was developed for that purpose.

It was found that by choosing suitable loads the noise power can be considerably reduced. This is a low cost solution to the problem, and is easy to accomplish. At the same time the ability to measure and simulate this type of problem is developed.

# OPSOMMING

---

**Sleutelwoorde:** transmissielyn, EMV, meeting

Hierdie tesis bied 'n oplossing vir 'n EMV probleem wat by 'n oopgroef myn ontstaan het. Ongewenste detonasies is veroorsaak deur onverwagte platvlakgolf straling. Hierdie probleem word as 'n bedraadingsstelsel, waar 'n belaste transmissielyn onder die invloed van platvlakgolfstraling verkeer, behandel.

Die transmissielyn terminasies word sistematies bokant beide ideale en nie-ideale grondvlakke gevarieër, en die ruisdrywing in die terminasies gemeet. Simulasies is met NEC4D, 'n Momentmetode frekwesiegebiedkode, en MTL\_SIM, 'n eendimensionele eindige element tydgebiedkode, uitgevoer. Die akuraatheid van die simulasies word getoets teen resultate van 'n sorgvuldige meetproses. As nie-ideale grondvlak is 'n diëlektriese medium met elektriese eienskappe soortgelyk aan dié van ware grond gebruik. 'n Stroomlyn meetopstelling is ontwerp om die elektriese eienskappe van die diëlektrikum te meet.

Resultate van simulasies en metings toon duidelik dat die korrekte keuse van transmissielyn terminasies is minimum ruisdrywing in die terminasies tot gevolg kan hê. Sodoende word 'n laekoste oplossing vir die spesifieke probleem daargestel terwyl insig in die oplossing van dié soort EMV-probleme in die algemeen verkry word.



## ACKNOWLEDGEMENTS

---

I would like to thank Prof. Reader for his help and support throughout the duration of this thesis. His active and positive approach to the work was extremely motivating.

I would also like to thank Wessel Crouwkamp, Peet Kruger and the rest of the staff at S.E.D for the manufacture of the equipment used, and the staff at the Department of Electrical and Electronic Engineering who were always available for quick ideas and insights.

Claudia Brendel is thanked for her support and for proof reading the drafts.

Finally, I wish to express my appreciation for the support that my family has given over the years.

# CONTENTS

INTRODUCTION .....	1
<b>1 PLANE WAVE AND TRANSMISSION LINE THEORY .....</b>	<b>3</b>
1.1 TRANSVERSE ELECTROMAGNETIC WAVE POTENTIALS. ....	4
1.1.1 Electric Scalar and Magnetic Vector Potentials. ....	4
1.1.2 TEM Waves .....	5
1.2 UNIFORM PLANE WAVES .....	8
1.2.1 Uniform Plane Wave Transmission in Free Space. ....	8
1.2.2 Plane Waves in Dielectrics With Loss. ....	9
1.2.3 Plane Wave Reflection off a Ground Plane .....	11
1.3 TRANSMISSION LINE THEORY .....	13
1.3.1 Transmission Equations. ....	14
1.3.2 Transmission Line Reflection and Transmission Coefficients. ...	18
1.4 A BRIEF DISCUSSION OF THE TIME-DOMAIN SIMULATION THEORY. .	18
1.4.1 Transverse Field Potentials .....	19
1.4.2 Per-Unit-Length Parameters. ....	22
1.4.3 Multiple Transmission Lines .....	22
1.4.4 Scattered Voltage in Transmission Lines. ....	24
1.5 CONCLUSION. ....	24
1.6 REFERENCES .....	25

<b>2</b>	<b>MATERIAL PROPERTY MEASUREMENTS .....</b>	<b>26</b>
2.1	TRANSMISSION AND REFLECTION COEFFICIENTS OF A MATERIAL SAMPLE .....	26
2.2	MATERIAL PROPERTY MEASUREMENT STRUCTURE .....	30
2.2.1	Analytic Field Distributions and Characteristic Impedance of Stripline .....	30
2.2.2	Visualisation of the Electric Potential and Field Distribution of Stripline .....	33
2.2.3	Length of Stripline .....	35
2.3	CALIBRATION OF THE STRIPLINE MATERIAL PROPERTY MEASUREMENTS .....	37
2.4	MATERIAL PROPERTY MEASUREMENTS .....	39
2.4.1	Verification Using a Known Material .....	39
2.5	CONCLUSION .....	42
2.6	REFERENCES .....	43
<b>3</b>	<b>RADIATION ROBUSTNESS EXPERIMENT .....</b>	<b>44</b>
3.1	INCREASED RADIATION ROBUSTNESS THROUGH CORRECT TERMINATION IMPEDANCE CHOICE .....	45
3.2	BASIC EXPERIMENTAL SETUP .....	46
3.3	DESCRIPTION OF THE SIMULATIONS .....	48
3.3.1	Frequency-Domain Code: NEC4D .....	48
3.3.2	Time-Domain Code: MTL_SIM .....	50
3.4	MEASUREMENT SETUP .....	54
3.4.1	Antenna Placement .....	54

3.4.2	Equipment Used. . . . .	54
3.4.3	Transmission Line Terminations . . . . .	55
3.4.4	Power Requirements for the Measurement . . . . .	56
3.4.5	Power Normalisation for Comparison . . . . .	57
3.4.6	Loading Variations. . . . .	57
3.5	WIRES ABOVE A PERFECTLY ELECTRICALLY CONDUCTING GROUND. . . . .	58
3.6	WIRES ABOVE A LOSSY GROUND . . . . .	62
3.7	CONCLUSION. . . . .	66
3.8	REFERENCES. . . . .	67
	<b>CONCLUSION. . . . .</b>	<b>69</b>
	<b>APPENDIX A. . . . .</b>	<b>A1</b>

# INTRODUCTION

---

Electromagnetic compatibility (EMC) research involves the study of equipment in its electronic environment, specifically with a view to preventing electromagnetic interference (EMI) between systems. It is a subject that will demand more and more attention as the density of electronics increases throughout the world. EMC work is industry driven, and thus solutions to EMC problems should be as simple and cost-effective as possible. Unfortunately specific problems often require unique solutions which are difficult for a non-specialist to find.

However, some problems have a more generic nature, and general EMC rules can be learnt from their solutions. In this thesis a generic problem derived from an industry problem is discussed, and a simple and cost-effective means of solving this type of problem is demonstrated.

The problem stems from an accident and a series of incidents in an open-bed mining system, shown in Fig. 1. A controller box is connected by long wires to a series of detonators, which are placed in shafts filled with liquid explosives. An unexpected source of radiation (perhaps a two-way radio) illuminates the wires. Under this illumination the individual strands of wire in the transmission line are raised to potentials relative to one another and to the ground. Power then flows to the ends of the transmission line, possibly interfering with the equipment, and causing premature detonation. The approach taken in this study is to attempt to divert the unwanted power flowing along the transmission lines away from the sensitive detonator, and to absorb it in the controller. It is assumed that the controller is insensitive to the unwanted power.

An important element in the study is the ground to which the controller and detonators are attached. It is necessary to demonstrate the effect that the real ground

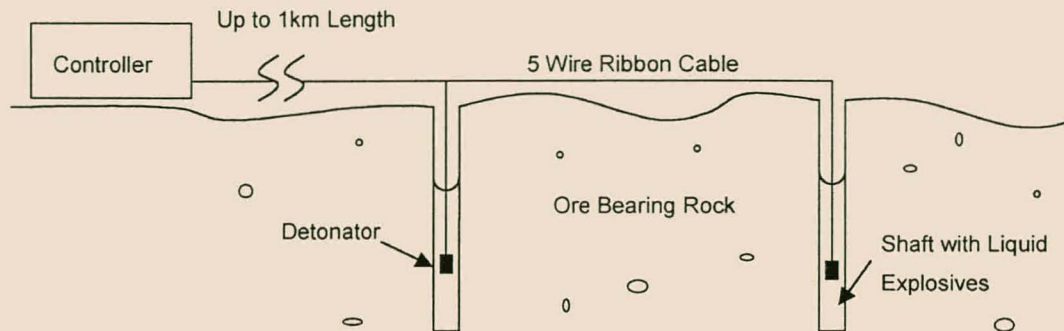


**Fig. 1. Digital System Subjected to Illumination**

has on the illumination power. For this reason an artificial lossy dielectric is constructed and its electrical properties are measured.

Chapter 1 develops an analytical understanding of transmission lines and electromagnetic waves. Although the theory of transverse electromagnetic (TEM) waves is well established, it is condensed here and from it the theory of plane waves and transmission lines is established. At the end of Chapter 1 the theory used by a transmission line simulation program is briefly examined.

The study makes use of wires stretched over either an ideal or a lossy ground. The measurements thus require a known artificial dielectric with loss. This in turn requires a system that can measure the electrical properties of materials over the frequency band of interest. Such a system is developed in Chapter 2.

Chapter 3 discusses the simulations and measurements of a loaded transmission line system subjected to illumination from a noise source. The results of the measurements confirm the ability of the simulation package to handle the loading above both an ideal and a lossy ground. A minimum in received power is also demonstrated, giving a simple rule-of-thumb for system designers to increase their system's radiation robustness.

# CHAPTER 1

---

## Plane Wave And Transmission Line Theory

Plane waves and transmission lines are used throughout the thesis, and form the basis for understanding the studied effects. The theory associated with plane waves and transmission lines is developed in this chapter. While Maxwell's equations are at the core of any analysis of electromagnetic problems, direct application of the equations is limited to simple geometrical shapes. Numerical approximations are required to deal with large problems of practical interest, and the numerical techniques used in this thesis are also briefly examined in this chapter.

Both plane waves and transmission line waves are forms of transverse electromagnetic (TEM) waves. TEM waves, as the name suggests, only have electric and magnetic field distributions transverse to the direction of travel. TEM waves are examined first in this chapter, as the subsequent theory is based on them.

Plane waves are used to introduce radiated power into the radiation robustness experiment of Chapter 3, and are perhaps the simplest form of TEM waves. Plane waves are TEM waves in a source free region, and have no local space-dependent field variation in the transverse directions.

Transmission lines have conductors that do not vary in one dimension, allowing unique simplifications to Maxwell's full three-dimensional equations. Transmission lines add boundary conditions to the general TEM theory that result in the guiding of the waves along the conductors. A TEM transmission line structure is used in Chapter 2 for the electrical characterisation of an artificial ground. In the radiation robustness experiment of Chapter 3, transmission lines above the ground guide TEM or quasi-

TEM waves to and from the terminations. Termination loading effects are also understood by studying the TEM wave relationships in the transmission line.

## 1.1 Transverse Electromagnetic Wave Potentials

As TEM waves are used to describe both plane waves and waves in transmission lines, general equations associated with TEM waves are developed first. It is often more convenient to deal with potentials rather than fields, so potentials are used to aid the analysis.

### 1.1.1 Electric Scalar and Magnetic Vector Potentials

The electric scalar potential  $\Phi$  and the magnetic vector potential  $\mathbf{A}$  are introduced into Maxwell's equations, and are related by the Lorenz gauge condition:

$$\mu\mathbf{H} = \nabla \times \mathbf{A} \quad (1.1)$$

$$\mathbf{E} = -\nabla\Phi - \frac{\partial\mathbf{A}}{\partial t} \quad (1.2)$$

$$\nabla \cdot \mathbf{A} = -\epsilon\mu \frac{\partial\Phi}{\partial t} \quad (1.3)$$

$\mathbf{H}$  is the magnetic field intensity,  $\mathbf{E}$  is the electric field intensity, and  $\epsilon$  and  $\mu$  the permittivity and the permeability of the medium. Throughout this section  $\mu$  should be read as  $\mu_0$  as only non-ferromagnetic materials are used.

Inserting these potentials into Ampère's law and Gauss' law leads to two three-dimensional wave equations that relate the electric and magnetic potentials to sources.

$$\nabla^2 \mathbf{A} - \mu\epsilon \frac{\partial^2 \mathbf{A}}{\partial t^2} = -\mu\mathbf{J} \quad (1.4)$$

$$\nabla^2 \Phi - \mu\epsilon \frac{\partial^2 \Phi}{\partial t^2} = -\frac{\rho}{\epsilon} \quad (1.5)$$



The sources on the right of (1.4) and (1.5) are  $\mathbf{J}$ , the current density, and  $\rho$ , the unpaired or free charge density.

The electric scalar potential  $\Phi$  and the magnetic vector potential  $\mathbf{A}$  have thus been introduced into Maxwell's equations, without any approximations. Equations (1.1) to (1.3) are the defining equations for the potentials, while equations (1.4) and (1.5) link the potentials to their sources.

### 1.1.2 TEM Waves

TEM waves by definition do not have electric or magnetic field components in the direction of travel, giving the restrictions

$$H_z = 0 \quad (1.6)$$

$$E_z = 0 \quad (1.7)$$

where the subscript  $z$  indicates the vector component in the direction of travel. To convert the restrictions on field intensities into restrictions on the field potentials, (1.6) and (1.7) are applied to the potential's definitions (1.1), (1.2) and (1.3)

$$\mathbf{A} = A_z \mathbf{i}_z \quad (1.8)$$

$$\frac{\partial A_z}{\partial z} = -\mu\epsilon \frac{\partial \Phi}{\partial t} \quad (1.9)$$

$$\frac{\partial \Phi}{\partial z} = -\frac{\partial A_z}{\partial t} \quad (1.10)$$

Equations (1.9) and (1.10) can be combined into two one-dimensional wave equations

$$\frac{\partial^2 \Phi}{\partial z^2} = \mu\epsilon \frac{\partial^2 \Phi}{\partial t^2} \quad (1.11)$$

$$\frac{\partial^2 A_z}{\partial z^2} = \mu\epsilon \frac{\partial^2 A_z}{\partial t^2} \quad (1.12)$$

[1, §12.1], solutions to which are of the general form

$$\Phi = f_1\left(t - \frac{z}{c}\right) + f_2\left(t + \frac{z}{c}\right) \quad (1.13)$$

$$A_z = f_3\left(t - \frac{z}{c}\right) + f_4\left(t + \frac{z}{c}\right) \quad (1.14)$$

$$c = \frac{1}{\sqrt{\mu\epsilon}} \quad (1.15)$$

where  $f_n$  is any function and  $c$  is the speed of propagation in the medium.

Equations (1.13) and (1.14) show that the electric and magnetic fields consist of two waves travelling at speed  $c$ , one travelling in the positive  $z$  direction and the other in the negative  $z$  direction. Equation (1.15) shows that the speed of propagation of TEM waves is set by the electrical characteristics of the medium  $\epsilon$  and  $\mu$ . The forms of the waves are given by the functions  $f_n$ , which are found by using the relationships between fields and sources given by (1.4) and (1.5).

Equations (1.4) and (1.5) link field potentials to their sources. In general,  $\Phi$  and  $\mathbf{A}$  must satisfy these three-dimensional wave equations, both containing the three-dimensional Laplacian  $\nabla^2$ . In the Cartesian co-ordinate system the Laplacian can be divided up into the transverse and axial components:

$$\begin{aligned} \nabla^2 &= \frac{\partial^2}{\partial x^2} + \frac{\partial^2}{\partial y^2} + \frac{\partial^2}{\partial z^2} \\ &= \nabla_{xy}^2 + \frac{\partial^2}{\partial z^2} \end{aligned} \quad (1.16)$$

Here  $z$  is the axial direction of propagation and  $\nabla_{xy}^2$  is the transverse component of the three-dimensional Laplacian. Separating the three-dimensional Laplacians in the wave equations (1.4) and (1.5) into transverse and axial components, and combining them with the one-dimensional TEM wave equations (1.11) and (1.12) and the TEM wave restrictions (1.8), (1.9) and (1.10) shows that the current and charge densities set the transverse field distributions:

$$\nabla_{xy}^2 \Phi = -\frac{\rho}{\epsilon} \quad (1.17)$$

$$\nabla_{xy}^2 A_z = -\mu J_z \quad (1.18)$$

Thus, although the axial dependence of the fields is that of a wave, the transverse dependence is the same as the two-dimensional quasistatic case [1, §14.2]. This result enables the analysis of a large range of problems using the simplifications of quasistatic analysis. Quasistatics are used later in this chapter to describe the field distribution of the wire in the radiation robustness experiment.

Assuming a sinusoidal excitation and using phasor notation, the one-dimensional wave equations (1.11) and (1.12) become one-dimensional Helmholtz equations. This takes the analysis into the frequency domain.

$$\frac{\partial^2 \Phi}{\partial z^2} = -\omega^2 \mu \epsilon \Phi = -k^2 \Phi \quad (1.19)$$

$$\frac{\partial^2 A_z}{\partial z^2} = -\omega^2 \mu \epsilon A_z = -k^2 A_z \quad (1.20)$$

$$k = \frac{\omega}{c} \quad (1.21)$$

Here  $k$  is the wave number and  $\omega = 2\pi f$  is the radian frequency.

Useful solutions to Helmholtz equations are exponentials. A solution of this form is

$$\Phi = K_1 e^{-jkz} + K_2 e^{+jkz} \quad (1.22)$$

$$A_z = K_3 e^{-jkz} + K_4 e^{+jkz} \quad (1.23)$$

where  $K_n$  are constants. Here the positive and negative travelling waves are separated into two phasors. Note that (1.22) and (1.23) are simply solutions to the two one-dimensional wave equations assuming sinusoidal excitation, and thus they agree with the general solutions (1.13) and (1.14), bearing in mind the phasor notation. The functions  $f_n$  in (1.13) and (1.14) are of the form

$$f_n(z) = K_n \exp(\pm jkz) \quad (1.24)$$

This format moves the field solutions into the frequency domain.

The restrictions of only having transverse field components greatly simplify the full Maxwell equations. The TEM restrictions on the definitions of the electric and magnetic potentials are given in (1.8) to (1.10). The transverse dependence of the field distributions being equivalent to the electroquasistatic case is demonstrated by (1.17) and (1.18) and is used later in this chapter. The general solutions to the Helmholtz equations are given by (1.22) and (1.23) and these also appear frequently throughout this chapter.

## 1.2 Uniform Plane Waves

Uniform plane waves are TEM waves that have no space-dependent variation in transverse field distributions and are thus the simplest TEM waves. Typically these waves are found far from a source, where the radial and azimuthal field dependencies have become insignificant.

### 1.2.1 Uniform Plane Wave Transmission in Free Space

The uniform plane wave case is simple enough that solutions can be found working directly with the fields. With constants as transverse field distributions, the electric and magnetic field relationships in Faraday and Ampère's laws simplify to only having partial derivatives against the axial direction and time. Assuming there is only an x-directed electric field, and using phasor notation, the relationships are:

$$\frac{\partial E_x}{\partial z} = -j\omega\mu H_y \quad (1.25)$$

$$\frac{\partial H_y}{\partial z} = -j\omega\epsilon E_x \quad (1.26)$$

Equations (1.25) and (1.26) can be combined to form Helmholtz equations, and the solutions are again taken as having exponential forms, as shown in (1.22) and (1.23):

$$E_x(z, t) = E_+ e^{-jkz} + E_- e^{jkz} \quad (1.27)$$

$$H_y(z, t) = \frac{1}{\eta_c} [E_+ e^{-jkz} - E_- e^{jkz}] \quad (1.28)$$

$$\eta_c = \sqrt{\frac{\mu}{\epsilon}} \quad (1.29)$$

where  $E_+$  and  $E_-$  are constants for the forward and backward travelling waves respectively,  $k$  is the wave number as defined in (1.21),  $z$  is the direction of propagation and  $\eta_c$  is the characteristic impedance of the medium, a ratio of electric field to magnetic field.

Equations (1.27) and (1.28) show that the electric field and the magnetic field are orthogonal to one another. The forward travelling electric and magnetic fields are set in a constant ratio of the characteristic impedance, while the negative travelling waves have a negative impedance ratio [2, §6.2]. The characteristic impedance is used in Chapter 2 to find the electrical characteristics of the medium.

## 1.2.2 Plane Waves in Dielectrics With Loss

Loss in dielectric materials occurs when there is conduction. This conduction can be either Ohmic conduction of free charge, or the movement of bound electrons in a dielectric. The loss in real ground is both Ohmic and dielectric. The loss occurring due to the movement of bound electrons is modelled by expanding the permittivity  $\epsilon$  to include an imaginary part. Thus

$$\epsilon = \epsilon' - j\epsilon'' \quad (1.30)$$

where  $\epsilon'$  is the permittivity of the dielectric, and  $\epsilon''$  models the movement of bound electrons in the dielectric.

The conservation of free charge relates current density to the electric field and can be combined with Ohm's law as:

$$\begin{aligned}\mathbf{J} &= \sigma \mathbf{E} + \frac{d}{dt} [(\epsilon' - j\epsilon'')\mathbf{E}] \\ &\equiv j\omega \left( \epsilon' - j\epsilon'' - j\frac{\sigma}{\omega} \right) \mathbf{E}\end{aligned}\quad (1.31)$$

with a sinusoidal excitation assumed and using phasor notation. If there is no need to differentiate between the Ohmic and the dielectric loss, the simplification can be made that

$$\epsilon'' = \frac{\sigma}{\omega} \quad (1.32)$$

and (1.31) reduces to

$$\mathbf{J} = j\omega(\epsilon' - j\epsilon'')\mathbf{E} \quad (1.33)$$

where the frequency independent part of the loss has now been included in the parameter  $\epsilon''$ . This can be done because both  $\epsilon''$  and  $\sigma$  are merely parameters used to model conductive effects, and their definitions can be altered to suit the situation.

A wave travelling through a lossy medium experiences phase delay and attenuation. This is understood by introducing the complex dielectric constant (1.30) into the equation for waves travelling through free space. The general solutions to the Helmholtz equations, (1.27) and (1.28), include exponential terms and a wave number. The wave number is altered by (1.30) to become

$$k = \omega \sqrt{\mu(\epsilon' - j\epsilon'')} \quad (1.34)$$

and the exponentials in (1.27) and (1.28) separate into two parts:

$$e^{-jkz} = e^{-\alpha z} \cdot e^{-j\beta z} \quad (1.35)$$

where

$$jk = \alpha + j\beta \quad (1.36)$$

separating the real (loss) part from the imaginary (phase) part of the now complex wave number. Equation (1.35) shows that the loss creates an exponential attenuation at a rate  $\alpha$ , and the phase of the wave also changes to the propagation constant  $\beta$ .

When the conductivity dominates the wave number the approximation

$$\frac{\sigma}{\omega} \gg \epsilon'' \quad (1.37)$$

can be made, where the relationship between  $\epsilon''$  and  $\sigma$  (1.32), has been used. The wave number becomes

$$e^{-jkz} = e^{-j\omega \sqrt{\frac{\mu\sigma}{j\omega}} z} = e^{-\frac{1}{\delta} z} \cdot e^{-j\frac{1}{\delta} z} \quad (1.38)$$

$$\delta = \frac{1}{\sqrt{\pi f \mu \sigma}} \quad (1.39)$$

$\delta$  is the skin depth of the medium, and is the depth by which the field strengths have reduced to 37% of the original values. The depth of the artificial dielectric block used in the radiation robustness experiment of Chapter 3 is chosen to be greater than the skin depth to avoid reflections from the bottom of the block interfering with the measurement.

### 1.2.3 Plane Wave Reflection off a Ground Plane

The radiation robustness experiment involves a vertically polarised uniform plane wave striking wires either directly, or by first reflecting off a ground plane. The mechanism for the reflection is studied in this paragraph. Fig. 1.1 shows a vertically polarised wave incident on a ground plane.

If the ground plane is a perfect conductor, the boundary conditions

$$E_{Tangential} = 0 \quad (1.40)$$

$$H_{Normal} = 0 \quad (1.41)$$

must apply. When a forward travelling wave impinges on perfect conductor, there will be scattering in such a way that the boundary conditions (1.40) and (1.41) are satisfied. There can be no transmission into a perfect conductor as no potential difference and thus no electric field can exist there.

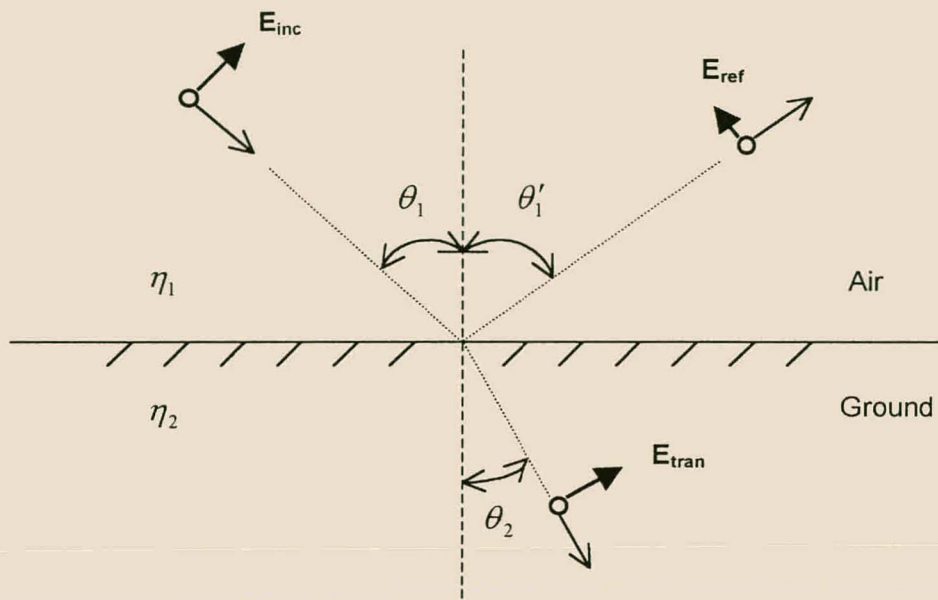


**Fig. 1.1 Vertically Polarised Plane Wave Reflection and Transmission at a Ground Plane**

If a vertically polarised wave strikes a ground plane at an angle  $\theta_1$  as shown in Fig. 1.1 the incident and reflected waves at the surface must add to give zero tangential electric field:

$$E_{tot} = E_{inc} \cos \theta_1 e^{-jkz \sin \theta_1} - E_{ref} \cos \theta'_1 e^{-jkz \sin \theta'_1} = 0$$

$$\Rightarrow \theta_1 = \theta'_1 \quad (1.42)$$

and

$$E_{inc} = E_{ref} \quad (1.43)$$

Thus the angle of incidence is equal to the angle of reflection, and the wave does not diminish in intensity. The electric field striking the wires can be up to twice as large as if the wires were in free space, as a reflected field and an incident field can add with constructive interference [2, §6.9].

When the wave strikes a dielectric surface, some of the wave is transmitted into the dielectric while the rest is reflected. At the point of contact the continuity conditions on the tangential components of the electric and magnetic fields must be satisfied.



This is possible only if

$$\begin{aligned} k_1 \sin \theta_1 &= k_1 \sin \theta_1' = k_2 \sin \theta_2 \\ \Rightarrow \theta_1 &= \theta_1' \end{aligned} \quad (1.44)$$

and

$$\frac{\sin \theta_2}{\sin \theta_1} = \frac{k_1}{k_2} = \frac{\sqrt{\mu_1 \epsilon_1}}{\sqrt{\mu_2 \epsilon_2}} \quad (1.45)$$

Equation (1.44) shows that the angle of incidence is still equal to the angle of reflection, while the angle of transmission into the dielectric is set by the material properties of the two media.

If the concept of wave impedance is used, transmission and reflection coefficients and wave impedance can be derived:

$$\gamma \equiv \frac{E_{ref}}{E_{inc}} = \frac{\eta_2 - \eta_1}{\eta_2 + \eta_1} \quad (1.46)$$

$$\tau \equiv \frac{E_{trans}}{E_{inc}} = \frac{2\eta_2}{\eta_2 + \eta_1} \quad (1.47)$$

$\gamma$  is the reflection coefficient, and  $\tau$  is the transmission coefficient. A wave illuminating a wire over a dielectric will strike the wires directly, have some reflected waves also striking the wire according to (1.46) and also penetrate the dielectric below the wire according to (1.47). These equations are used for the reflection coefficient approximations for the time-domain simulations of Chapter 3.

### 1.3 Transmission Line Theory

Transmission lines also support TEM waves, but add boundary conditions that guide the waves along conductors. The resulting equations are similar to the uniform plane wave equations. However, the presence of the conductors gives extra degrees of freedom that are used in Chapter 2 to create a material property measurement system.

The time-domain simulation code uses transmission line theory to simplify Maxwell's equations. Although approximations are made, this leads to very fast simulation

times, and the full three-dimensional equations are reduced to one-dimensional equations.

### 1.3.1 Transmission Equations

A transmission line is a structure that guides waves by placing boundary conditions on the transverse field distributions. An ideal transmission line consists of two or more perfect electrical conductors which have no variation in their cross-section, and which are infinitely long. The expected field distributions are TEM waves because of the high conductivity of the conductors, low frequencies of interest and the invariance along the length of the transmission lines. For a TEM wave, the electric and magnetic field intensity must be zero along the transmission line, leaving the vector potential with only an axial component, as shown in (1.8).

Additional boundary conditions (BC) are that the tangential electric field and the normal magnetic field must be zero at the surface of the conductors as given by (1.40) and (1.41). These BC show that the waves are still TEM, but unlike the plane wave, the transverse field distributions in transmission lines are set by the conductor's cross-section geometry, using the inhomogeneous equations (1.17) and (1.18).

The transverse field distributions can be found using quasistatic principles on the specific geometry involved, while the space-dependent wave dynamics occur only in the axial direction. Once the electric and magnetic potentials are known the wave behaviour can be described in terms of voltages and currents. It is useful to define per-unit-length parameters to describe the relationships between voltage and charge (capacitance) and current and magnetic flux (inductance). Electroquasistatics is used to find the capacitance per unit length, and magnetoquasistatics is used to find the inductance per unit length. The per-unit-length parameters are defined as

$$C_\ell \equiv \frac{\rho_\ell}{V} \quad (1.48)$$

$$L_\ell \equiv \frac{\lambda_\ell}{I} \quad (1.49)$$

$C_\ell$  is the capacitance per unit length,  $\rho_\ell$  is the charge per unit length,  $V$  is the potential difference between the conductors,  $L_\ell$  is the inductance per unit length,  $\lambda_\ell$  is the flux linkage per unit length and  $I$  is the current flowing in one of the wires.

By inverting (1.17) and (1.18) the Poisson equations are derived:

$$A_z = \frac{\mu}{4\pi} \int \frac{J_z}{|\mathbf{r} - \mathbf{r}'|} dv' \quad (1.50)$$

$$\Phi = \frac{1}{4\pi\epsilon} \int \frac{\rho_v}{|\mathbf{r} - \mathbf{r}'|} dv' \quad (1.51)$$

$\mathbf{r}$  is a distance vector from the origin to the charge or current, and  $\mathbf{r}'$  is a distance vector from the origin to the observation point. If these equations are evaluated on one of the conductors of a transmission line, a relationship between the per-unit-length parameters and the medium surrounding the conductors is found to be

$$L_\ell C_\ell = \frac{A_z \lambda_\ell}{I \Phi} = \mu\epsilon \quad (1.52)$$

This result allows the transmission line to be characterised by an evaluation of the per-unit-length inductance only, or vice versa. If the medium around the conductors is homogeneous (1.52) can be used to find the other parameter.

If the transmission line is a two-conductor system, boundary conditions can be evaluated on both of the conductors, leading to transmission equations. If the boundary conditions are no flux linkage and no voltage per unit length on the one conductor, and there is a flux linkage  $\lambda_\ell$  and a voltage  $V$  per unit length on the other, these boundary conditions can be inserted into (1.9) and (1.10). Using the relationships between the per-unit-length parameters and the charge and current densities (1.47), (1.48) and (1.52) leads to the telegrapher's equations [2, §5.2]

$$\frac{\partial V}{\partial z} + L_\ell \frac{\partial I}{\partial t} = 0 \quad (1.53)$$

$$\frac{\partial I}{\partial z} + C_\ell \frac{\partial V}{\partial t} = 0 \quad (1.54)$$

The telegrapher's equations (1.53) and (1.54) describe the evolution of TEM waves in a transmission line, and are a subset of the more general TEM relationships between electric and magnetic potentials, equations (1.9) and (1.10). The waves are described in terms of voltages, currents, and per-unit-length parameters. The time-domain simulations of Chapter 3 use modified forms of these equations, which are discussed later in this chapter.

The telegrapher's equations describe the electrical behaviour of one unit length segment of the transmission line. This unit cell is shown in Fig. 1.2 and consists of a per-unit-length shunt capacitance and a per-unit-length series inductance. A voltage source  $V_G$  is included in the unit cell to model the effect of the radiating wave in the radiation robustness experiment of Chapter 3.

Combining and solving (1.53) and (1.54) gives a general set of solutions to the one-dimensional wave equations, as was found with uniform plane waves in (1.27) and (1.28).

$$V(z, t) = F_1\left(t - \frac{z}{c}\right) + F_2\left(t + \frac{z}{c}\right) = V_+ + V_- \quad (1.55)$$

$$I(z, t) = \frac{1}{Z_c} \left[ F_1\left(t - \frac{z}{c}\right) - F_2\left(t + \frac{z}{c}\right) \right] = \frac{1}{Z_c} [I_+ - I_-] \quad (1.56)$$

$$c = \frac{1}{\sqrt{L_\ell C_\ell}} \quad (1.57)$$

$$Z_c = \sqrt{\frac{L_\ell}{C_\ell}} \quad (1.58)$$

$c$  is the speed of transmission,  $Z_c$  is the characteristic impedance of the line and the positive and negative subscripts refer to the positive and negative travelling waves along the  $z$  axis respectively.

The relationship between the per-unit-length parameters and the electrical characteristics of the medium (1.52), combined with (1.57), shows that permittivity and permeability of the medium set the speed of transmission, as was the case of the plane wave. From (1.52) and (1.58) it is shown that the conductor geometry and the

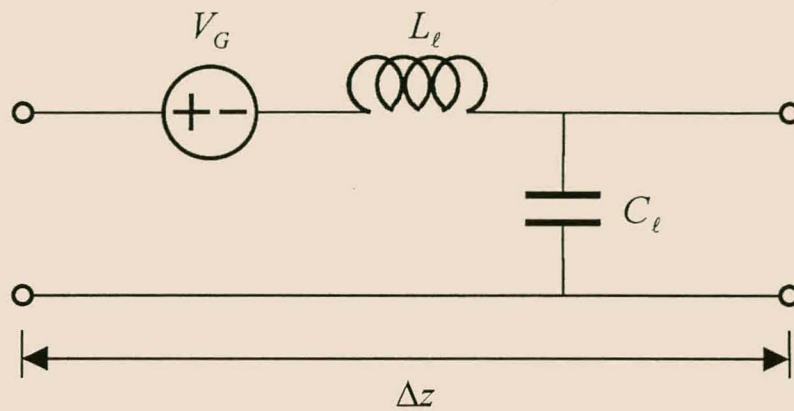


**Fig. 1.2. Ideal Transmission Line Unit Cell**

medium surrounding the conductors set the characteristic impedance of the transmission line. This forms the basis for the material property measurements in Chapter 2.

The general solutions to the telegrapher's equations, (1.55) to (1.58), show that the transmission line will transmit any voltages and currents at the speed of light (in the medium) to its terminations. The total voltages and currents are the summation of positive and negative travelling waves. Just as the electric and magnetic fields have a ratio set by the characteristic impedance of the medium (1.29), the transmission line has a characteristic impedance set by the ratio of voltage to current in (1.58).

In order to move into the frequency domain, exponentials are inserted in the solutions (1.55) and (1.56), and phasor notation is used. These have the same form as for the plane waves, (1.22) and (1.23).

$$V = V_+ e^{-jkz} + V_- e^{jkz} \quad (1.59)$$

$$I = \frac{1}{Z_c} [V_+ e^{-jkz} - V_- e^{jkz}] \quad (1.60)$$

Here  $k$  is the wave number as defined in equation (1.21), and includes the properties of the medium surrounding the conductors.

### 1.3.2 Transmission Line Reflection and Transmission Coefficients

An abrupt impedance change in a transmission line causes reflections of the TEM waves. This impedance change can be caused by a termination on the transmission line, or a change in the geometry of the conductors, or a change in the electrical characteristics of the medium surrounding the conductors. If the change in the transmission line is from a characteristic impedance  $Z_c$  to an impedance  $Z_L$ , then reflection and transmission coefficients can be found from the solutions to the telegrapher's equations (1.55) and (1.56).

$$\Gamma \equiv \frac{V_-}{V_+} = \frac{Z_L - Z_c}{Z_L + Z_c} \quad (1.61)$$

$$T \equiv \frac{V_L}{V_+} = \frac{2Z_L}{Z_L + Z_c} \quad (1.62)$$

$\Gamma$  is the reflection coefficient,  $T$  the transmission coefficient and  $V_L$  is the voltage at the section with  $Z_L$  characteristic impedance [2, §5.4]. These equations are familiar from plane wave theory, (1.46) and (1.47). In Chapter 2 equations (1.61) and (1.62) are used to deduce the electrical properties of an artificial dielectric.

## 1.4 A Brief Discussion of the Time-Domain Simulation Theory

Although numerical simulations are used to analyse the behaviour of the fields in the radiation robustness experiment, it is important to understand the theory underlying the simulations. Understanding this theory leads to the avoidance of some basic simulation errors. Basic ideas that form the building blocks for the time-domain simulation package are derived here.

First the per-unit-length parameters of round wires are derived, using the potentials introduced earlier in this chapter. Then the multiple transmission line matrices are introduced, followed by a discussion of the approach used in the time-domain simulation package to include the effect of illumination by a plane wave.

In the radiation robustness experiment transmission lines are round perfect electrical conductor (PEC) wires stretched parallel to a ground, shown in cross-section Fig. 1.3. If the ground plane is also a PEC, an image wire appears below the surface of the ground.

There is neither wire sag and nor variation in the ground height, making the system invariant along the length of the wire, and the wire is treated as if it were infinitely long, so that end effects can be ignored. The medium surrounding the wire is uniform in permittivity ( $\epsilon$ ) and permeability ( $\mu$ ).

The actual conductor and the image conductor form a two-conductor system. The per-unit-length parameters are deduced from quasistatic case.

### 1.4.1 Transverse Field Potentials

In order to find the electric field distribution, the wires are treated as if they are open circuited at one end and driven by an ideal voltage source at the other. This creates an electroquasistatic situation, with the wires holding equal but opposite charges. The capacitance per unit length is found from the electric field distribution.

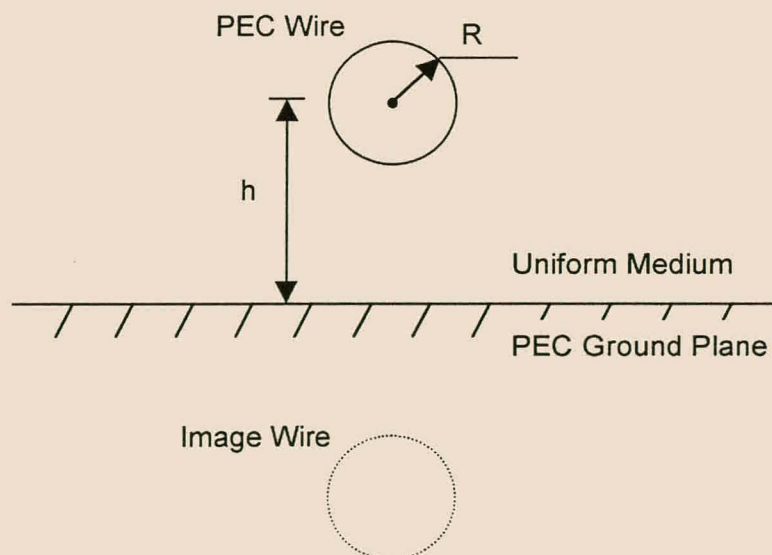


Fig. 1.3. Cross-Section of a Round Wire Above a Ground Plane



The potentials are found by first replacing the round metal wires, which are right cylinders, with line charges. The wire and its image have equal but opposite charges, and the same holds true for the line charges replacing them. The electric field from the positive line charge is found using Gauss' law and rotational symmetry arguments

$$\mathbf{E} = \frac{\rho_\ell}{2\pi\epsilon} \cdot \frac{1}{r_+} \mathbf{i}_{r_+} \quad (1.63)$$

$\rho_\ell$  is the charge per unit length,  $r_+$  the radial distance from the positive line charge and  $\mathbf{i}_{r_+}$  the unit vector pointing away from the positive line charge [1, §1.3].

The quasistatic transverse dependence of the fields simplifies the relationship between the potentials and the electric field (1.2) to

$$\mathbf{E} = -\nabla\Phi \quad (1.64)$$

[1, §4.5] and the potential from the positive line charge ( $\Phi_+$ ) is found by inverting (1.64) and using (1.63):

$$\begin{aligned} E_{r_+} &= -\frac{\partial\Phi_+}{\partial r_+} \\ \Rightarrow \Phi_+ &= -\frac{\rho_\ell}{2\pi\epsilon} \cdot \ln\left(\frac{r_+}{r_0}\right) \end{aligned} \quad (1.65)$$

where  $r_0$  is a reference radius brought in as a constant of integration [1, §4.6].

The total potential is the superposition of the two equal but oppositely charged lines, with the negatively charged line's potential ( $\Phi_-$ ) found in the same way as the positive line charge potential. The reference radii are chosen as equal, leading to their cancellation.

$$\begin{aligned} \Phi &= \Phi_+ + \Phi_- \\ &= \frac{\rho_\ell}{2\pi\epsilon} \ln\left(\frac{r_-}{r_+}\right) \end{aligned} \quad (1.66)$$

where  $r_-$  is the radial distance from the negative line charge.



The equipotential surfaces can be found by setting (1.66) equal to a constant  $C$ . Converting to Cartesian co-ordinates leads to a quadratic function of  $x$  and  $y$ .

$$x^2 + d^2 + 2dy \frac{1+k^2}{1-k^2} + y^2 = 0 \quad (1.67)$$

In (1.67)  $2d$  is the distance between the line charges and  $k = \exp\left(\frac{2\pi\epsilon C}{\rho_\ell}\right)$ .

The equipotential surfaces are thus circular, with the circle centres offset from the line charges. Any one of the surfaces can be replaced by a perfectly electrically conducting cylinder without changing the potentials outside that cylinder. Thus the potential created by two perfectly electrically conducting cylinders is identical to the potential created by offset line charges.

If the wire is a height  $h$  above the ground plane and the radius of the wire is  $R$  (as shown in Fig. 1.3), then the locus for the equipotentials and the locus for the cylinder relate the position of the line charges to the position of the wires and (1.66) becomes

$$\Phi = -\frac{\rho_\ell}{2\pi\epsilon} \ln\left(\frac{h}{R} + \sqrt{\left(\frac{h}{R}\right)^2 - 1}\right) \quad (1.68)$$

This is the electric field potential for a wire above a perfectly conducting ground plane.

In most cases the radius of the wire is much smaller than its height above the ground, and the approximation  $\frac{h}{R} \gg 1$  reduces (1.68) to

$$\Phi = -\frac{\rho_\ell}{2\pi\epsilon} \ln\left(\frac{2h}{R}\right) \quad (1.69)$$

This approximation is used by the time domain simulation package.

The magnetic vector potential is found by creating a magnetoquasistatic situation in the two-wire system. The wires are driven by a current source on one end and loaded on the other end by a short circuit. Image theory is used and the cylindrical wires are

replaced by line currents. The potential is found in a similar way to the electric potential as

$$A_z = -\frac{\mu}{2\pi} I \ln\left(\frac{2h}{R}\right) \quad (1.70)$$

where  $I$  is the current flowing in one of the wires.

### 1.4.2 Per-unit-length Parameters

The per-unit-length capacitance and inductance can be calculated from the scalar potential in (1.69) and the vector potential in (1.70). Capacitance per unit length is given by

$$\begin{aligned} C_\ell &\equiv \frac{\rho_\ell}{V} \\ &\approx \frac{2\pi\epsilon}{\ln\left(\frac{2h}{R}\right)} \end{aligned} \quad (1.71)$$

where  $V$  is the potential difference between the wire and the ground plane [1, §4.6].

The inductance per unit length is derived in a similar way:

$$\begin{aligned} L_\ell &\equiv \frac{\lambda_\ell}{I} \\ &\approx \frac{\mu}{2\pi} \ln\left(\frac{2h}{R}\right) \end{aligned} \quad (1.72)$$

[1, §8.6]

These equations are used by a pre-processor for the time-domain simulation package to find the per-unit-length parameters [4].

### 1.4.3 Multiple Transmission Lines

The treatment of multiple transmission lines extends the technique used to find the potentials of the single wire above a ground. Image theory shows that there will be interaction between all the conductors and all their images. The principle of superposition of the potentials still applies, so the problem becomes one of

summation. The interaction with an image conductor, however, will have a sign change. Thus if there are  $n$  conductors, matrices of inductances and capacitances per unit length can be created, using (1.71) and (1.72).

$$[C_\ell] = \begin{bmatrix} C_{11} & C_{12} & \cdot & \cdot \\ C_{21} & \cdot & \cdot & \cdot \\ \cdot & \cdot & \cdot & \cdot \\ \cdot & \cdot & \cdot & C_{nn} \end{bmatrix} \quad (1.73)$$

$$C_{ij} = \frac{2\pi\epsilon}{\ln\left(\frac{d_{ij}}{d'_{ij}}\right)} \quad (1.74)$$

$$C_{ii} = \frac{2\pi\epsilon}{\ln\left(\frac{2h_i}{R}\right)} \quad (1.75)$$

where  $d_{ij}$  is the distance between wire  $i$  and wire  $j$ , a prime indicates distance to an image conductor, and all radii are assumed equal. Note that when there are  $n$  wires there are  $n - 1$  propagation modes, which experience different effective permittivities in a non-homogeneous medium. This leads to different propagation velocities for the different modes.

Inductances are found in the same way and the inductance matrix is

$$[L_\ell] = \begin{bmatrix} L_{11} & L_{12} & \cdot & \cdot \\ L_{21} & \cdot & \cdot & \cdot \\ \cdot & \cdot & \cdot & \cdot \\ \cdot & \cdot & \cdot & L_{nn} \end{bmatrix} \quad (1.76)$$

$$L_{ij} = \frac{\mu}{2\pi} \ln\left(\frac{d_{ij}}{d'_{ij}}\right) \quad (1.77)$$

$$L_{ii} = \frac{\mu}{2\pi} \ln\left(\frac{2h_i}{R}\right) \quad (1.78)$$

with the notation as above [3, §6.5].

### 1.4.4 Scattered Voltage in Transmission Lines

If a transmission line is illuminated by a plane wave, the line will scatter the voltage so that on its surface the tangential electric field and the normal magnetic fields are zero. Following the scattered voltage solution by Agrawal [3, §8.2.2], the line current and the scattered voltage are treated as the unknowns rather than the total voltage. The excitation fields consist of the incident field and the reflected field.

The scattered voltage of the line is given by

$$V^{scat} = - \int_{-h}^h E_y^{scat} dy \quad (1.79)$$

where  $E_y^{scat}$  is the vertical electric field created by the scattering of the real wire and the image wire.

Applying Faraday's law and Ampere's law to infinitesimal surfaces and separating the fields into excitation and scattered fields leads to telegrapher's equations expressed in terms of the total current and the scattered voltages:

$$\frac{dV^{scat}}{dz} + L_\ell \frac{dI}{dt} = V_{S1} \quad (1.80)$$

$$\frac{dI}{dz} + C_\ell \frac{dV^{scat}}{dt} = 0 \quad (1.81)$$

$$V_{S1} = \int E_y^{ex} dy = \int E_y^{inc} + E_y^{refl} dy \quad (1.82)$$

Thus the telegrapher's equations (1.53) and (1.54) are altered to include a voltage source term along the wire. This source term  $V_S$  is found by integrating the vertical excitation electric field between the ground plane and the wire [3, §7.2].

## 1.5 Conclusion

In this chapter the theory that forms the base for the rest of the thesis is derived from Maxwell's equations. The electric scalar and magnetic vector potentials are introduced as they are easily found from a structure's geometry, and subsequent equations can be derived from them. The wave phenomena are understood in terms of TEM waves, themselves based on the electric and magnetic potentials.

Transmission lines are seen as structures that guide TEM waves, and transmission and reflection coefficients are derived from TEM wave behaviour.

Although the theory derived in this chapter is well established, it is still of use to condense it here, as a strong mathematical base is created for the subsequent chapters. This allows these chapters to focus on the topics at hand, rather than having to shift between fundamental theory and specific results. The origin of and relationships between the basic equations are also clarified when they are derived together.

This chapter also looks at the theory on which the one-dimensional finite-difference time-domain code is based. It is necessary to examine the theory underlying this code, as its techniques are far less widely used than, for example, the frequency-domain method-of-moments code, to which it is compared in Chapter 3. At the same time the theory in this paragraph shows the approach an analytical solution to this problem would take. The complexity of the problem suggests that simulations are necessary, especially when there is a lossy ground.

## 1.6 References

- [1] H.A. Haus, J.R. Melcher, *Electromagnetic Fields and Energy*, Prentice-Hall, 1989.
- [2] S. Ramo, J.R. Whinnery, T. van Duzer, *Fields and Waves in Communication Electronics 3<sup>rd</sup> Edition*, John Wiley & Sons, 1994.
- [3] F.M. Tesche, M.V. Ianoz, T. Karlsson, *EMC Analysis Methods and Computational Models*, John Wiley & Sons, 1997.
- [4] J. van der Merwe, *Users Guide for MTL\_Sim*, Department of Electrical and Electronic Engineering, September 1998.

## CHAPTER 2

---

# Material Property Measurements

The radiation robustness experiment requires measurements above an ideal ground and a lossy ground. While a good approximation to the ideal ground can be manufactured easily from sheets of metal, the lossy ground must be made from an artificial dielectric that has similar electrical properties to soil. This artificial dielectric is created by coating polystyrene balls with graphite. Unfortunately the process is not very repeatable and each batch has different electrical properties. Thus a material property measurement system is required to determine these properties. A system was developed that uses the reflection and transmission coefficients of TEM waves in transmission lines in order to establish the permittivity and conductivity of the artificial dielectrics.

## 2.1 Transmission and Reflection Coefficients of a Material Sample

Any transmission line's characteristic impedance is a function of conductor geometry and the medium surrounding the conductors. For the material property measurements the conductor geometry is fixed, leaving the characteristic impedance a function of the medium only. From (1.58), the characteristic impedance of the transmission line will change from  $Z_0$  (when the conductors are in free space) to

$$Z_M = \sqrt{\frac{\mu_r}{\epsilon_r}} Z_0 = \sqrt{\frac{1}{\epsilon_r}} Z_0 \quad (2.1)$$

when the conductors are surrounded by some dielectric medium with  $\epsilon_r$  relative permittivity. The artificial dielectric is a non-ferromagnetic material and thus  $\mu_r$  is 1.

Fig. 2.1 shows a transmission line with a material sample surrounded by air. For the purposes of these measurements, air can be treated as free space. Included in Fig. 2.1 is an S-parameter representation of the system. These parameters relate reflections from and transmission through the material sample to the measurements made using an automatic network analyser (ANA).

If there is a transition along the transmission line from free space to the material of interest, there is a reflection coefficient that is a function of the electrical properties of the material only. The reflection coefficient is given by combining (1.61) with (2.1):

$$\Gamma_M = \frac{\sqrt{\frac{\mu_r}{\epsilon_r}} - 1}{\sqrt{\frac{\mu_r}{\epsilon_r}} + 1} \quad (2.2)$$

where  $\Gamma_M$  is a reflection coefficient at the air-material interface, as shown in Fig. 2.1. In order to solve for both the permittivity and the permeability, a second independent equation is required. This second equation comes from the transmission coefficient through the material sample.

Transmission through a material is given by (1.62), repeated here with the relative permittivity and permeability included.

$$T_M = e^{-j\frac{\omega}{c}\sqrt{\mu_r\epsilon_r}\ell} \quad (2.3)$$

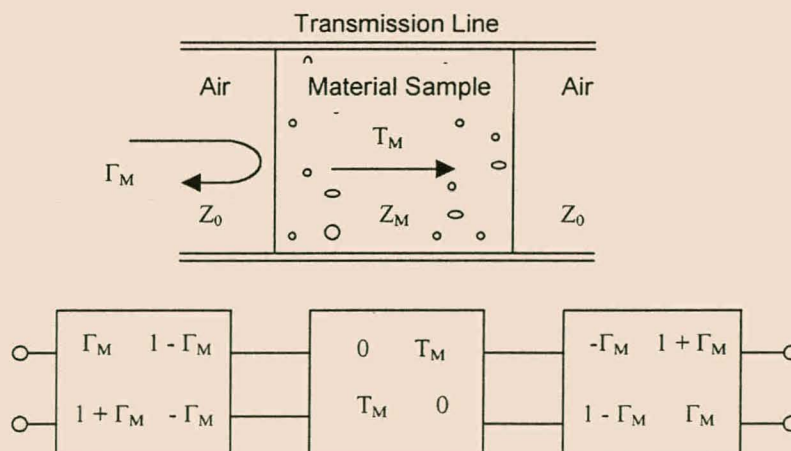


Fig. 2.1. Transmission Line with Material Sample

$T_M$  is the transmission coefficient through the material,  $\omega$  is the frequency in radians per second,  $c$  is the speed of light in free space, and  $\ell$  is the length of the material sample.

A 2-port measurement can be made, and using simple flow-diagram analysis  $S_{11}$  and  $S_{21}$  can be related to  $\Gamma_M$  and  $T_M$  using the S-parameter blocks shown in Fig. 2.1.

$$S_{11} = \frac{(1 - T_M^2)\Gamma_M}{1 - T_M^2\Gamma_M^2} \quad (2.4)$$

$$S_{21} = \frac{(1 - \Gamma_M^2)T_M}{1 - T_M^2\Gamma_M^2} \quad (2.5)$$

These equations can be inverted to solve for the reflection and transmission coefficients [1]:

$$\Gamma_M = \frac{(1 - S_{21})^2 S_{11}}{1 - S_{11}^2 S_{21}^2} \quad (2.6)$$

$$T_M = \frac{(1 - S_{11})^2 S_{21}}{1 - S_{11}^2 S_{21}^2} \quad (2.7)$$

When  $\Gamma_M$  and  $T_M$  are known, equations (2.2) and (2.3) can be solved simultaneously to find  $\epsilon_r$  and  $\mu_r$ . Equations (2.2) and (2.3) are inverted to find [2]

$$\frac{\mu_r}{\epsilon_r} = \left( \frac{1 + \Gamma_M}{1 - \Gamma_M} \right)^2 = x \quad (2.8)$$

$$\mu_r \epsilon_r = -\frac{c^2}{\omega^2 \ell^2} [\ln|T_M| + j(\text{Arg}(T_M) + 2\pi n)]^2 = y \quad (2.9)$$

According to [2],  $n$  in (2.9) can be estimated from the group delay. The ambiguity arises when the material sample is longer than a wavelength in the material. The group delay can be estimated by assuming that  $\epsilon_r$  and  $\mu_r$  do not change rapidly with frequency. The group delay for the  $i^{\text{th}}$  frequency point is given by

$$\tau_i = \ell \cdot \frac{d}{df} \left( \frac{\sqrt{\epsilon_r \mu_r}}{\lambda_0} \right) \quad (2.10)$$



$$\approx \frac{\ell}{f_i - f_{i-1}} \left[ \frac{\sqrt{\epsilon_r \mu_r}}{\lambda_0} \Big|_{f_i} - \frac{\sqrt{\epsilon_r \mu_r}}{\lambda_0} \Big|_{f_{i-1}} \right] \quad (2.11)$$

$\lambda_0$  is the wavelength in free space and  $f_i$  and  $f_{i-1}$  are the  $i^{\text{th}}$  frequency and the  $i-1^{\text{th}}$  frequency respectively. The actual group delay is measured, and the correct root  $n$  is found when

$$\tau_n - \tau_{\text{actual}} \approx 0 \quad (2.12)$$

To find the initial permittivity and permeability,  $n$  is assumed zero for the low frequencies where the material sample is known to be shorter than a wavelength.

Equations (2.8) and (2.9) are solved simultaneously:

$$\epsilon_r = \sqrt{\frac{y}{x}} \quad (2.13)$$

$$\mu_r = \sqrt{x \cdot y} \quad (2.14)$$

Only the positive root is used as the real parts of the relative permittivity and permeability must be larger than +1. In general both  $\epsilon_r$  and  $\mu_r$  can be complex, but for the purposes of the radiation robustness experiment magnetic materials will not be used, and  $\mu_r$  will be expected to be unity. If the assumption of unity  $\mu_r$  is made, (2.8) can be used to directly to find  $\epsilon_r$ . This allows a single measurement of the reflection coefficient to give the permittivity and conductivity of the material, as (2.8) is becomes a function of one variable only.

The permittivity and conductivity of the material are found from (2.13) and (1.30):

$$\begin{aligned} \epsilon_r \cdot \epsilon_0 &= \epsilon' - j\epsilon'' \\ &\approx \epsilon' - j\frac{\sigma}{\omega} \end{aligned} \quad (2.15)$$

where  $\epsilon_0$  is the permittivity of free space,  $\epsilon'$  is the permittivity of the material sample,  $\sigma$  is the conductivity of the sample and  $\omega$  is the frequency in radians per second.

## 2.2 Material Property Measurement Structure

In order to implement equations (2.1) and (2.2) a TEM mode transmission line with a fixed geometry is required. An open structure would allow material samples to be inserted with ease, and the structure would also need to be able to connect to a network analyser. Such a structure is stripline, shown in cross-section in Fig. 2.2.

The characteristic impedance of stripline should be close to  $50 \Omega$  (with an air fill), so that connection to a  $50 \Omega$  network analyser causes minimal reflection. Using the magnetic and electric potentials discussed in Chapter 1, an approximate characteristic impedance of the stripline structure can be found analytically. This analysis does not take the actual thickness  $t$  into account. For greater accuracy a numerical technique would be required, but this was not considered necessary. However, a simple numerical technique was developed to aid visualisation of the field distributions. The visualisation shows that energy does not leak out of the open edges of the stripline.

### 2.2.1 Analytic Field Distributions and Characteristic Impedance of Stripline

It is of interest to show how the principles developed in Chapter 1 are used to find the potential distributions and thus the characteristic impedance of the stripline.

By approximation a stripline can be modelled as two parallel plate transmission lines

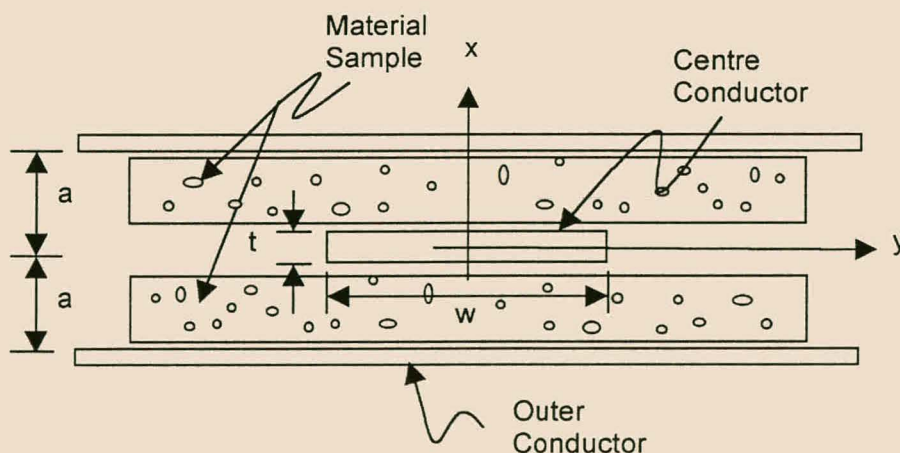


Fig. 2.2. Stripline Geometry in Cross-Section

on top of one another [4, §8.6]. This analysis ignores the finite thickness of the centre conductor.

The characteristic impedance of a single parallel plate transmission line is found by solving (1.17) and (1.18). This is done in combination with the boundary conditions of no voltage on the one conductor and a voltage  $V$  on the other, and a current  $I$  flowing on each. These equations are applied to the top and bottom plates [3, Ex. 14.2.1].

$$A_z = \frac{a\mu}{w} \left(1 - \frac{x}{a}\right) I \quad (2.15)$$

$$\Phi = \left(1 - \frac{x}{a}\right) V \quad (2.16)$$

$A_z$  is the magnetic vector potential in the  $z$  direction and  $\Phi$  is the electric potential.  $I$  and  $V$  are the current and voltages set by the boundary conditions. The characteristic impedance is found from the capacitance and inductance per unit length. Equation (1.49) relates the inductance per unit length to (2.15), while (1.52) relates the inductance per unit length to the capacitance per unit length:

$$C_\ell = \frac{\epsilon w}{a} \quad (2.17)$$

$$L_\ell = \frac{\mu a}{w} \quad (2.18)$$

The characteristic impedance for a single parallel plate transmission line is

$$Z_c = \frac{a}{w} \sqrt{\frac{\mu}{\epsilon}} \quad (2.19)$$

By connecting the two identical transmission lines in parallel any transmitted power is shared evenly, halving the characteristic impedance:

$$Z_c = \frac{a}{2w} \sqrt{\frac{\mu}{\epsilon}} \quad (2.20)$$

Material samples can easily be cut to half a centimetre, which sets the separation parameter  $a$ . For a stripline with  $50 \Omega$  impedance with an air filling, the width, from (2.20), is  $w \approx 19$  mm. Although this is a rough approximation, the principles used in finding the field distributions are well demonstrated.

A more accurate formula for the characteristic impedance of stripline requires conformal mapping techniques [4, §8.6]. This analysis still ignores the finite thickness of the centre conductor. With the limitation

$$\frac{w}{2a} > 0.56 \quad (2.21)$$

an elliptic integral in the solution can be approximated and the characteristic impedance is given by:

$$Z_c \approx \frac{\pi \sqrt{\frac{\mu}{\epsilon}}}{8 \ln \left[ 2 \exp \left( \frac{\pi w}{4a} \right) \right]} \quad (2.22)$$

With the separation set to 5 mm and the characteristic impedance set to 50  $\Omega$ , the width is found as  $w = 14.4$  mm. The rough approximation ( $w \approx 19$  mm) compares poorly to this more accurate analysis, so the conformal mapping technique was used in the design.

The finite thickness of the conductor alters the characteristic impedance of the stripline, although neither (2.20) nor (2.22) take this into account. The result is that the characteristic impedance of the line is not exactly known. However, if it is reasonably close to 50  $\Omega$ , it will not cause large reflections at the interface.

It was found that calibration and measurements were extremely sensitive to variations in the height of the centre conductor. The thickness of the centre conductor was thus set to  $t = 1$  mm for mechanical strength.

A numerical technique can be used to visualise the electric field distribution in the stripline, including the effect of a finite thickness centre conductor. This is useful as it can show whether the bulk of the fields travel through the material sample, and whether energy is leaking out of the open sides of the structure.

## 2.2.2 Visualisation of the Electric Potential and Field Distribution of Stripline

In order to find the transverse field distribution of a transmission line with arbitrary cross-section, equations (1.17) and (1.18) need to be solved numerically. The spatial derivatives are approximated using second order Taylor expansions:

$$\Phi(x+h, y) \approx \Phi(x, y) + h \frac{\partial \Phi(x, y)}{\partial x} + \frac{h^2}{2} \frac{\partial^2 \Phi(x, y)}{\partial x^2} \quad (2.23)$$

$$\Phi(x-h, y) \approx \Phi(x, y) - h \frac{\partial \Phi(x, y)}{\partial x} + \frac{h^2}{2} \frac{\partial^2 \Phi(x, y)}{\partial x^2} \quad (2.24)$$

where  $h$  is any small distance from a point of interest. Combining (2.23) and (2.24) results in the approximation for the second order derivatives against  $x$  in (1.17) and (1.18):

$$\frac{\partial^2 \Phi(x, y)}{\partial x^2} = \frac{\Phi(x+h, y) - 2\Phi(x, y) + \Phi(x-h, y)}{h^2} \quad (2.25)$$

A similar approximation can be made for the derivatives in the  $y$  direction, and equation (1.17) can be approximated by

$$\Phi(x+h, y) + \Phi(x-h, y) + \Phi(x, y+h) + \Phi(x, y-h) - 4\Phi(x, y) = -\frac{\rho h^2}{\epsilon} \quad (2.26)$$

In a source free region, the potential at a point  $(x, y)$  is given by

$$\Phi(x, y) = \frac{\Phi(x+h, y) + \Phi(x-h, y) + \Phi(x, y+h) + \Phi(x, y-h)}{4} \quad (2.27)$$

Thus by dividing the transmission line cross-section into an equally spaced grid the potential at any node must be the average of the potentials of its surrounding nodes [4, §1.20]. This process can be carried out recursively by a computer. This process is limited to regions bounded by fixed potentials, as (2.27) does not take the effect of the potential at infinity into account.

A routine was written in MATLAB in order to solve (2.27). The routine is listed in Appendix A. A two-dimensional matrix is used to represent the grid of potentials. A second matrix marks the boundary conditions so that they are not altered during the averaging process.



A test case with an analytical solution [3, §5.5] was used to verify the code. The example is a closed box with a lid at potential above the sides and base, shown in Fig. 2.3. The result of the run is also shown in the figure. The solid lines are the equipotentials, while the arrows represent the electric field, with length proportional to the strength of the field. The numerical solution replicates the field distribution found analytically in Haus and Melcher. It should be noted that visualisation, rather than numerical accuracy, is desired from this numerical technique.

The electric field distribution of a cross-section of stripline was computed. The centre conductor is 14.4 mm wide and 1 mm thick, while the top and bottom conductors were chosen to be 5 cm wide. The right half of the stripline structure's electric potential and field distributions are shown in Fig. 2.4.

The strongest electrical fields are at the edges of the centre conductor, where there is unfortunately not likely to be any uniform section of the material sample. However, the bulk of the fields do travel between the centre conductor and the top and bottom plates. Note that the electric field dies away as it approaches the edge of the stripline, indicating that energy is not leaking out of the sides.

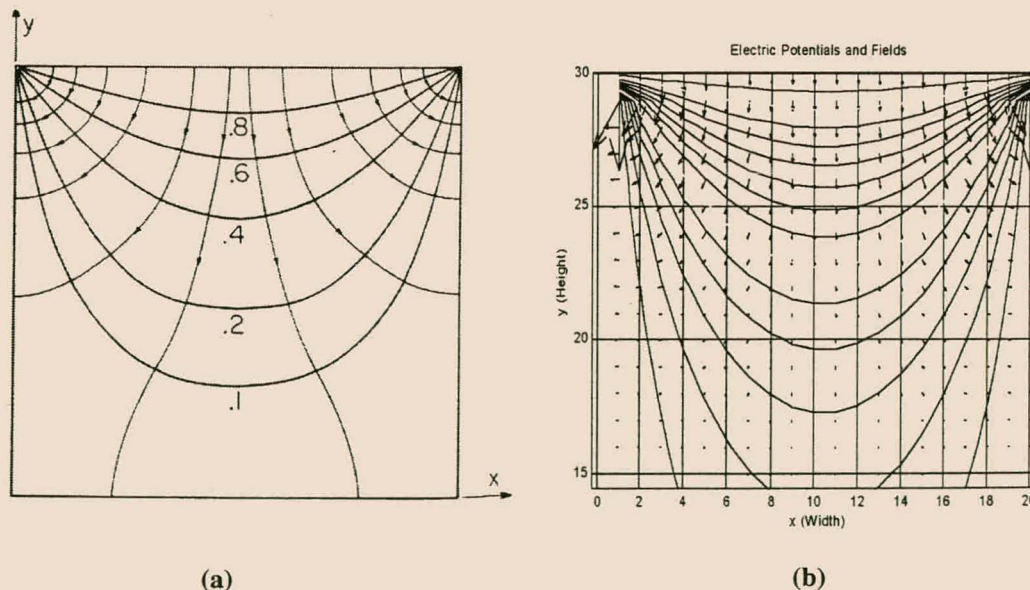


**Fig. 2.3. Closed Box with Lid at a Potential Above the Bottom and Sides (a) Analytical Result from [3, §5.5] (b) Numerical Approximation Result**

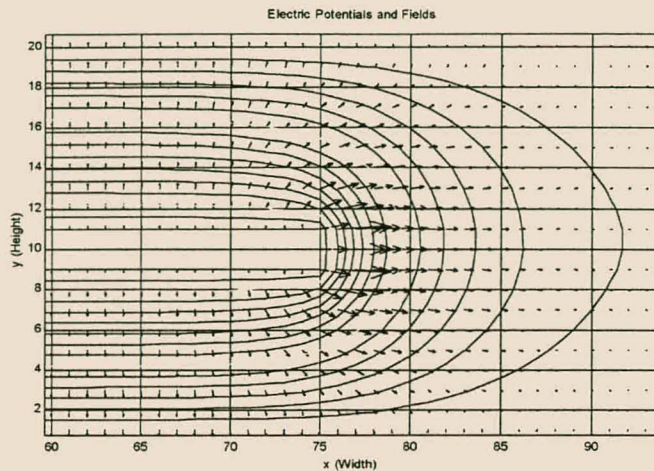


Fig. 2.4. Numerical Electric Potential and Field Distribution – Right Half of Stripline

### 2.2.3 Length of the Stripline

The final design parameter is the length of the stripline. The stripline was designed to have enough travel time to allow for time gating of a pulse from the front face of the material sample. Such time gating would allow direct measurement of the reflection coefficient  $\Gamma_M$ . However, the width of the pulse is also related to the bandwidth, demanding a high bandwidth for a narrow pulse.

The stripline supports TEM waves from D.C. to just below the cut-off frequencies of the first modes in the parallel plane transmission lines discussed in §2.1. Thus the maximum measurement frequency is set by the width of the inner conductor, according to the formula [4, §8.3]

$$f_c = \frac{mc}{2w} \quad (2.28)$$

where  $f_c$  is the cut-off frequency,  $c$  is the speed of light in the medium,  $w$  is the width of the inner conductor, and  $m$  is the mode number. With  $m$  set to 1, the cut-off frequency is related to the relative dielectric permittivity by

$$f_c \approx \frac{10.4 \times 10^9}{\sqrt{\epsilon_r}} \quad (2.29)$$

The artificial ground has an expected relative dielectric permeability of approximately 2, giving a cut-off frequency of more than 7 GHz.

The length of the stripline was chosen to allow time gating of the reflections off the front face of the material. The length of the sample was chosen to be larger than 15 cm. The shortest time for a reflected pulse to travel the 30 cm return distance would be in air, with a time of approximately 1 ns. The length of a time pulse available from the HP8510 ANA using Fourier transforms can be calculated as

$$t_{-6dB} = \frac{0.6}{f_{span}} \times 1.6 \quad (2.30)$$

[5, p3.5-16] which, with a span of 5 GHz, is 0.213 ns. In equation (2.30) the rise time of the pulse sets the numerator, and the shape of the pulse sets the multiplication factor to 1.6. This pulse shape is 'normal', one of the available choices on the ANA.

Time gating can be performed with this frequency span. The total length of the stripline was chosen to be 35 cm, leaving 10 cm on either side of the material sample free. This extra distance is included to reduce the effect of evanescent modes which are below cutoff.

The junction between the coaxial cables and the stripline was made by tapering the stripline centre conductor, in order to reduce reflections. 3.5 mm Standard Military Adapter (SMA) connectors were used to feed the stripline structure.

Table 2.1 lists the dimensions of the stripline structure, and Fig. 2.5 shows these final dimensions.

**Table 2.1. Dimensions of the Stripline Structure**

Centre Conductor Width ( $w$ )	14.4 mm
Separation ( $a$ )	5 mm
Top and Bottom Conductor Widths	0.5 cm
Length of Stripline	35 cm



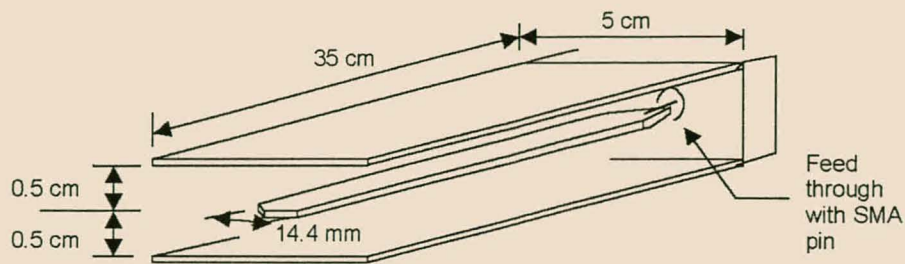


Fig. 2.5. Stripline Geometry

## 2.3 Calibration of the Stripline Material Property Measurements

A 1-port error adapter model is shown in Fig. 2.6 [5, p2.1-1]. The model shows that between the measured ( $S_{11M}$ ) and the actual ( $S_{11A}$ ) reflection coefficients, there are three unknowns introduced by the automatic network analyser (ANA), cables and the coaxial to stripline junction. The relationship is given by

$$S_{11M} = E_D + \frac{S_{11A} E_R}{1 - E_S S_{11A}} \quad (2.31)$$

Measurement of the three independent standards creates three independent equations, allowing the error coefficients to be found.

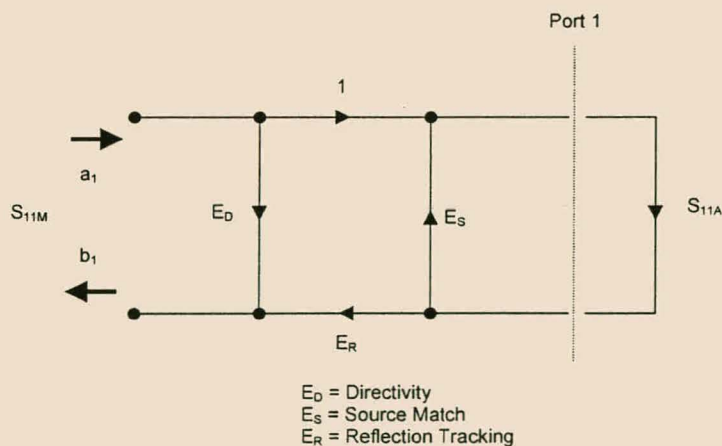


Fig. 2.6. One – Port Error Model

The calibration of the stripline consists of inserting known loads into the stripline at known positions. The ANA then measures these loads and calculates the error coefficients. The internal calibration of the stripline was performed using a short, an offset short and a sliding load. The short was machined, while the sliding load was cut out of dielectric absorber, as shown in Fig. 2.7.

Because the calibration standards are made from two separate pieces, great care was taken during calibration to align the top and bottom pieces correctly. A clamp was also used to ensure good contact between the short and the stripline.

It is difficult to construct a good load in the stripline, as this would involve a long taper. By using a sliding load the need for a well matched load is avoided. Instead of a single measurement of a good load, a poor load is shifted along the stripline at least five times and measured. As the load remains constant (though poor) the only difference between the successive measurements is the phase change caused by the varying distance travelled by a wave to the load and back. The ideal load can be estimated from these measurements. However, the amount of phase change decreases as frequency drops, limiting the accuracy of the calibration at lower frequencies.

An HP8510 ANA was used for the internal calibration. The calibration kit description was altered on the HP8510 for the new calibration standards. The full 2 port

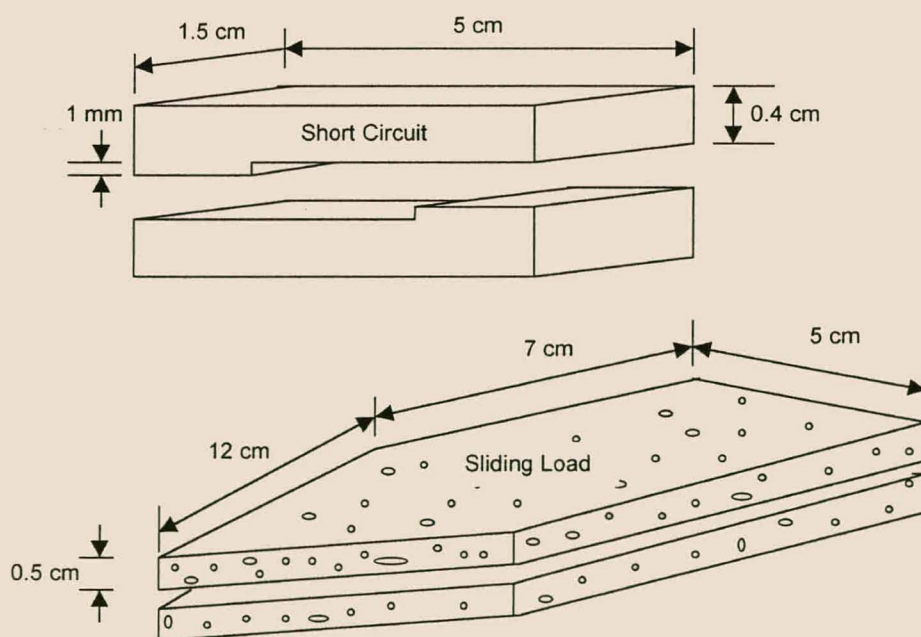


Fig. 2.7. Short Circuit and Sliding Load Calibration Standards

calibration requires a “through” standard, which was set to 15 cm, keeping the calibration 9 cm away from the co-axial to stripline conversion where some non-TEM fields are excited.

## 2.4 Material Property Measurements

It was necessary to confirm the quality of the measurements by first measuring a known material. The material had to be lossy so as to be similar to the artificial ground. The measurement of expected values allowed confident measurement of the artificial ground properties.

### 2.4.1 Verification Using a Known Material

In order to verify the stripline measurement technique a “phantom dielectric” with known electrical properties was used [7]. This material has electrical characteristics similar to human muscle. It thus has a high relative permittivity (due to muscle’s high water content) and high conductivity. The phantom dielectric is a viscous liquid, so the stripline needed to be watertight. It was turned on its side, and styrofoam stoppers and tape were used to seal a chamber. The chamber was then filled with the liquid. Styrofoam stoppers were used as they have electrical properties very similar to air or free space, and could thus be ignored during the measurement.

For the internal calibration the stoppers interfered with the sliding load and had to be moved to the ends of the stripline, only 1 cm away from the coaxial to stripline junction. A comparison of the expected and measured values of permittivity and conductivity are shown in Fig. 2.8 and 2.9. As the material has a high loss the signal transmitted through the sample was attenuated to become unmeasurable. The material properties were thus extracted from a one-port measurement of the initial reflection only.

Unfortunately there are only three frequencies at which the material properties are known. The highest of these compares well to the measurement, although the lower frequency points differ. The measurements show a plateau between 1 GHz and 4 GHz, and it is assumed that the best measurement values are achieved in this region. The poor measurement results below 1 GHz are as result of the poor quality of the sliding load. The measurement resonance at near 5 GHz on all the measurements is

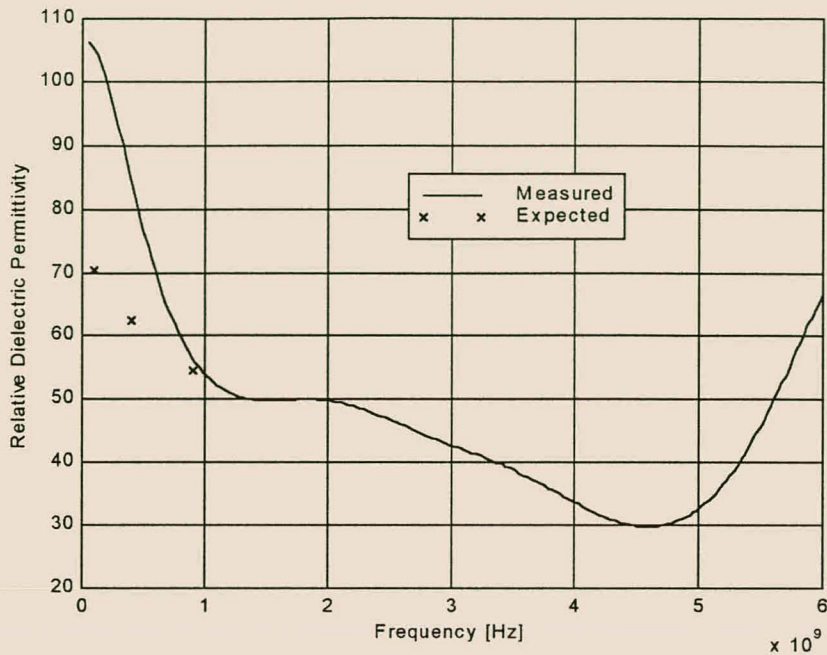


**Fig. 2.8. Comparison of Expected and Measured Dielectric Permittivity of a Known Material**

caused by a half-wavelength resonance between the short and the offset short during calibration.

The accurate measurement of the known material allowed measurements of the artificial dielectric to be made with reasonable confidence. Results of the measurement are shown in Fig. 2.10 and 2.11.

The simulations require only one value of permittivity and conductivity to cover the entire band. The values of permittivity and conductivity were chosen where the graphs plateau, at approximately 2.5 GHz. The measured electrical parameters of the artificial dielectric at this frequency point are given in Table 2.2.

**Table 2.2 Permittivity and Conductivity of the Lossy Ground**

$\epsilon_r$	1.7
$\sigma$	0.04 S/m



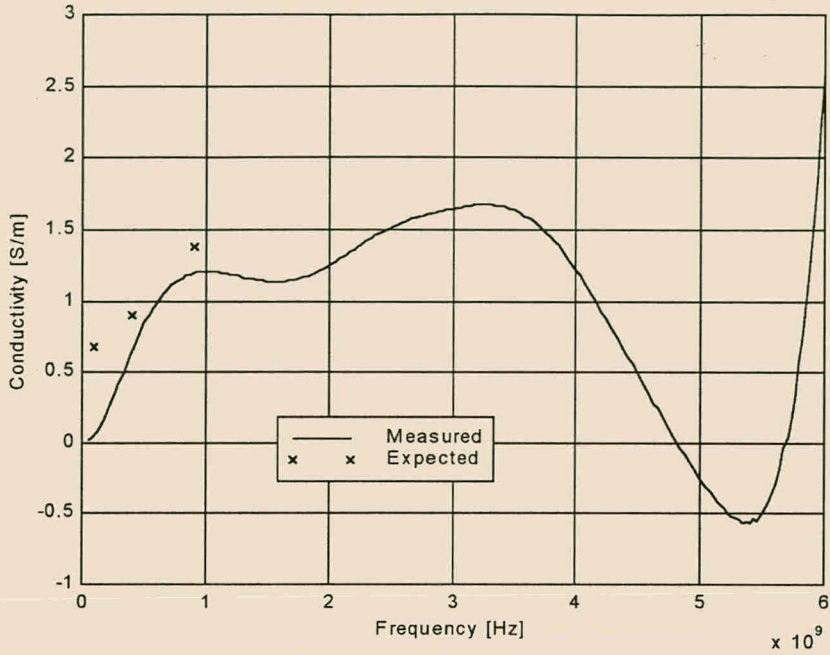


**Fig. 2.9. Comparison of Expected and Measured Conductivity of a Known Material**

The artificial dielectric was measured independently in a system in a band above 10 GHz. The low frequency electrical permittivity and conductivity were estimated from extracted parameters [8]. The results of this measurement compare well with the

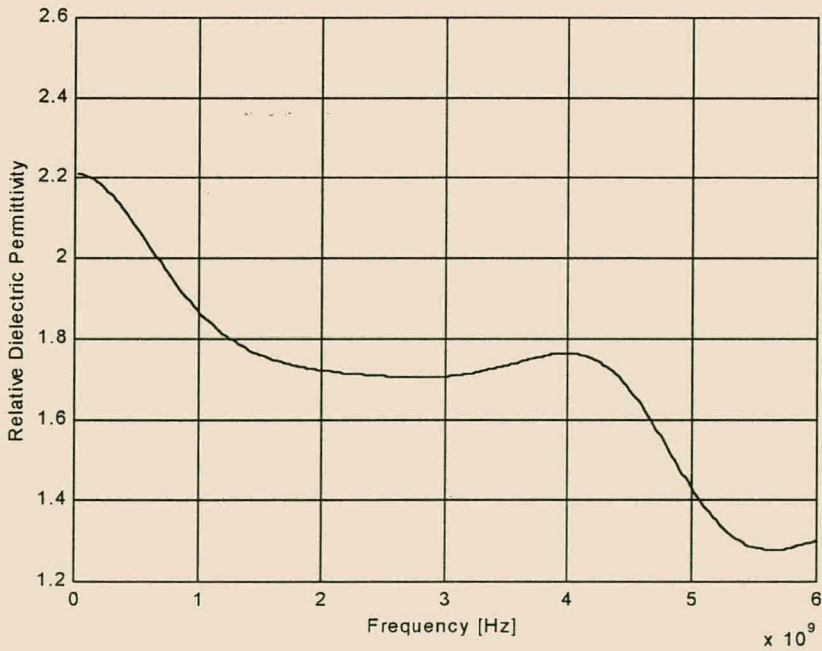


**Fig. 2.10. Measured Permittivity of the Artificial Dielectric**

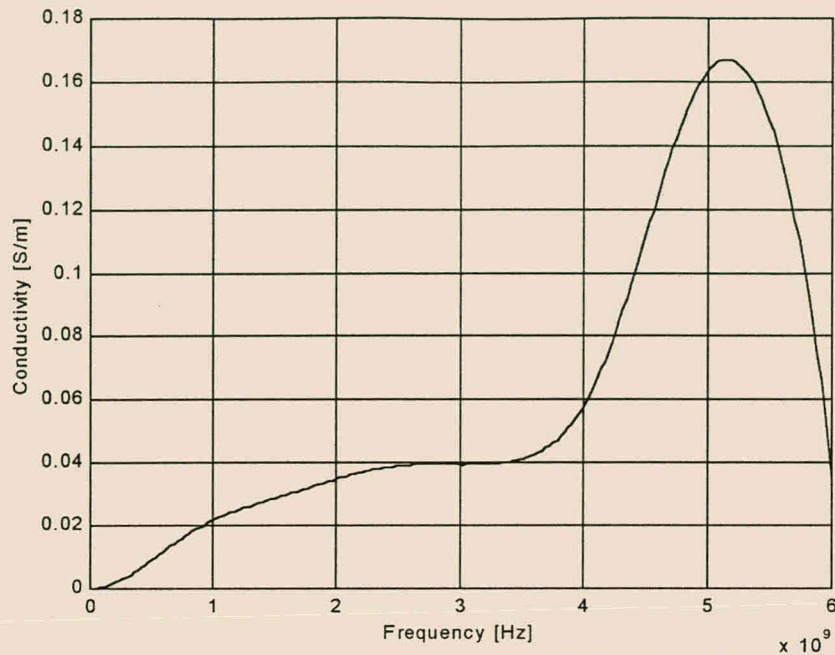


**Fig. 2.11. Measured Conductivity of the Artificial Dielectric**

results of the stripline system, with the values  $\epsilon_r = 1.7$  and  $\sigma = 0.143$  S/m when extrapolated to low frequencies. The difference between the high frequency system and the stripline conductivities could be as result of the extrapolation.

## 2.5 Conclusion

Principles of TEM waves discussed in Chapter 1 were used to create a material property measurement system. Difficulties in making these measurements centre on the calibration and error removal. Confirmation of the quality of the measurements was made by measuring a known material, and there is confidence in the values obtained for the artificial soil.

The low frequencies of the measurement are limited by the sliding load. Although [6] reports that the highest quality calibration is performed using three offset shorts, this technique was not successful, as resonances were found across the band. The high frequency limit on the measurement is set by the distance between successive short circuit placements in the stripline.

According to references in [9], the electrical parameters for dry soil are  $\epsilon_r \approx 3$  and  $\sigma \approx 0.001 - 0.01$  S/m. The artificial dielectric thus has a conductivity similar to dry soil, but a relative dielectric constant of approximately half the real soil value. However, the permittivity is different enough from free space so that its effects play significant roles in the simulations and measurements. Once the ability to handle a ground with a non-unity permittivity has been demonstrated, confidence can be had in future simulations using more accurate values for the electrical parameters for soil.

## 2.6 References

- [1] Hewlett-Packard Product Note 8510-3, "Materials Measurement – Measuring the Dielectric Constant of Solids with the HP8510 Network Analyser".
- [2] W.B. Weir, "Automatic Measurement of Complex Dielectric Constant and Permeability at Microwave Frequencies," *IEEE Proc.*, vol. 62, no. 1, pp. 33-36, Jan. 1974.
- [3] H.A. Haus and J.R. Melcher, *Electromagnetic Fields and Energy*, New Jersey: Prentice Hall, 1989.
- [4] S. Ramo, J.R. Whinnery, T. van Duzer, *Fields and Waves in Communication Electronics, 3rd Ed.*, John Wiley and Sons, 1994.
- [5] Hewlett – Packard HP8510B + 24D, *Student Guide for Basic Network Measurements Using the HP8510B Network Analyser System*, Ed.3.0, Jan. 1988.
- [6] B. Bianco, A. Corana, S. Ridella and C. Simicich, "Evaluation of Errors in Calibration Procedures for Measurements of Reflection Coefficient," *IEEE Trans. Instrum. Meas.*, vol. IM-27, pp.354-358, Dec. 1978.
- [7] G. Hartsgrove, A. Kraszewski and A. Surowiec, "Simulated Biological Materials for Electromagnetic Radiation Absorption Studies," *Bioelectromagnetics*, vol. 8, pp. 29-36, 1987.
- [8] M. Bingle, I.P. Theron and J.H. Cloete, "A Frequency Domain Dispersion and Absorption Model for Numerically Extracting the Constitutive Parameters of an Isotropic Chiral Slab from Measured Reflection and Transmission Coefficients," *Conference Proceedings of 13<sup>th</sup> Annual Review of Progress in Applied Computational Electromagnetics*, Monterey C.A., p803, March 1997
- [9] C.A. Balanis, *Advanced Engineering Electromagnetics*, John Wiley & Sons, 1989.

## CHAPTER 3

---

# Radiation Robustness Experiment

The radiation robustness experiment aims to provide a low-cost method of reducing a system's vulnerability to noise from an external radiation source. As described in the Introduction, the problem reveals itself in the premature detonations in an open cast mining explosives system. A controller and a series of detonators are low power digital circuits connected by long transmission lines and the ground. While the prevention of premature detonation of the explosives in this specific system is desired, a more generally applicable solution to a generic wiring problem is of interest for electromagnetic compatibility (EMC) issues.

The generic EMC problem is shown in Fig. 3.1. It is a circuit with a driver and receiver connected by a transmission line and ground, and subjected to plane wave illumination from a noise source. The power in the plane wave is picked up by the transmission line, which acts as an antenna. This noise power is then transported by the transmission line to its terminations, potentially causing system failure and damage.

In order to reduce the system's vulnerability to this radiation it is desirable to reduce the amount of noise power on the receiver side of the transmission line. It is assumed that the driver side is not vulnerable to this noise, as it is not a sensitive device. Although the receiver circuit is typically a voltage-measuring device, the radiation robustness experiment aims to reduce the noise power rather than the noise voltage. The noise voltage can be determined from the noise power and the termination impedance.



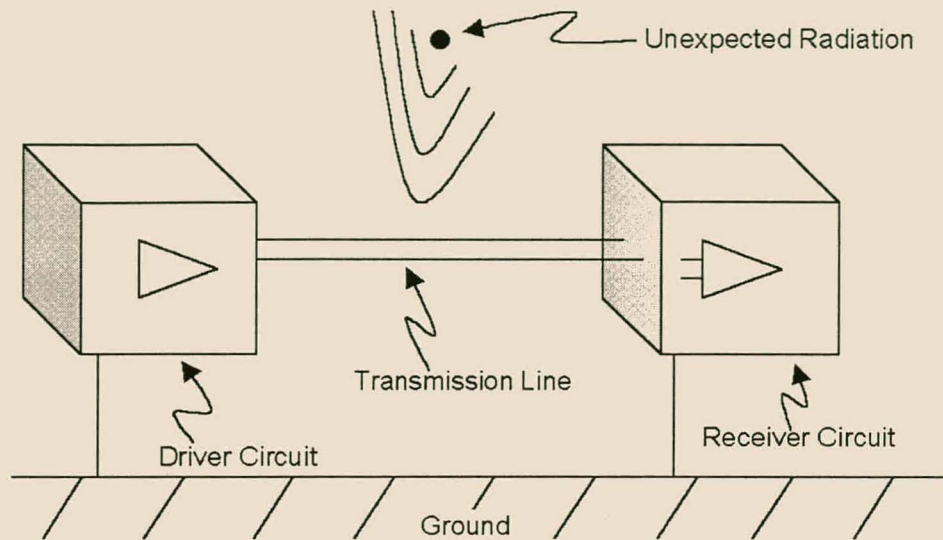


Fig. 3.1. Low Power System Subjected to Plane Wave Illumination

### 3.1 Increased Radiation Robustness Through Correct Termination Impedance Choice

A cheap and effective way to reduce the noise power at the receiver circuit is to alter the driver and receiver input and output impedances. These impedances are typically chosen during the digital design phase of the system in order to reduce the over-all power requirements. Thus the driver circuit is given a low output impedance and the receiver circuit is given a high input impedance. As the radiation robustness experiment shows, this is a particularly poor choice for system radiation robustness – the high reflection coefficients at either end cause large voltages and currents to flow along the transmission line.

The experiment uses both a highly conducting (metal) ground and a more realistic (lossy dielectric) ground. Although the open cast mining system is always above a real ground, the ideal ground is of interest for the simplifications it brings to the simulations. Simulations of structures above a perfectly conducting ground can be modelled as two symmetrical structures – the original structure and its image in the ground plane. Thus the simulations are of two structures in free space, which doubles the problem size but does not decrease the accuracy. The simulation of

structures above a real half plane involves a number of approximations and numerical integration that reduces the accuracy of the simulation.

The radiation robustness experiment thus consists of systematically varying the load terminations of a transmission line subjected to radiation, in order to find a minimum in the power received in the terminations. Measurements are made above an ideal and a lossy ground to establish the validity of simulation methods. Simulations are then used vary the impedances in order to find a noise power minimum.

If the system in question is a digital system, as is the case of the open cast mining system, a noise voltage minimum is required, rather than a noise power minimum. On the other hand, other systems could have sensors that require noise current or noise power minima. The simulation results of this chapter can be converted to the appropriate parameter with the knowledge of the power and the impedance at the termination. Thus the terminations that give a noise power minimum in this chapter might not be the best choice for every system, and the correct graph should be used.

## 3.2 Basic Experimental Setup

The experiment setup is based on a series of multiconductor transmission line measurements made by J. van der Merwe in his doctoral thesis [1]. Thus the basic setup for the radiation robustness experiment was chosen to make full use of the measurements already performed.

The transmission line wires are stretched taut above a ground plane by two vertical plates. The wires are approximately 2m long, cut to the exact distance between the fixtures on either side. The radius and spacing of the wires are taken directly from the actual open cast mining explosives system. The mining explosives system uses 5 wires in a flat ribbon sheath. However, in this experiment the sheath is removed and only two wires are used, each of which is terminated to ground. This is done to simplify the problem while keeping the multiconductor nature of the industry system. The wires are stretched above the ground at a height that is convenient for attaching cables to the SMA connectors. Table 3.1 lists the transmission line geometry parameters:

**Table 3.1. Transmission Line Parameters used for the Radiation Robustness Experiment**

Parameter	Value
Length of Transmission Line	1.96 m – 2 m
Number of Conductors	2
Separation between Wires	2.5 mm
Radius of Wires	0.4 mm
Height of Wires above Ground	14.5 mm
Dielectric Sheath	None

The depth of the dielectric block used for the lossy ground sets the lowest frequency that can be measured with this setup. The incident radiated power penetrates the block and can reflect off the bottom of the block to interfere with the experiment. According to J. van der Merwe, it can be assumed that if 37 % of the incident power reaches the bottom surface, the amount of power reflected back to the top of the dielectric block is small enough not to interfere with the experiment. The skin depth, derived in §1.2.2, is given as:

$$\delta = \frac{1}{\sqrt{\pi f \mu \sigma}} \quad (3.1)$$

The depth of the block is approximately 30 cm, which sets the lowest frequency to approximately 70 MHz, as the conductivity is 0.04 S/m (Table 2.2). This frequency is much lower than a radiation source used in the radiation robustness experiment. Thus the low frequency of the radiation robustness experiment is set by the lowest frequency of the antenna, instead of by this constraint. The antenna has a minimum frequency of 500MHz, and is described in more detail later in this chapter.

The distance between the wires and the ground plane sets the highest frequency. For transmission line TEM modes, this height must be much smaller than a wavelength. Keeping the distance less than a tenth of a wavelength gives

$$f_{\max} = \frac{c}{\lambda_{\min}} < \frac{c}{10 \cdot h} \quad (3.2)$$

$$< 2.07 \text{ GHz}$$

Thus the maximum frequency is chosen as 2 GHz.

The radiation robustness experiment thus uses the frequency range 500 MHz – 2 GHz. This covers both the cellular telephone frequencies and television frequencies. It should be noted that once the ability to measure and simulate this type of problem has been demonstrated, a wider frequency band can be simulated with confidence.

### 3.3 Description of the Simulations

Simulations were run using both time and frequency domain codes. The frequency domain code, NEC4D [2], is a well-established code that is used as a standard for comparison to the time-domain simulation. The time-domain code, MTL\_SIM, is a multiconductor transmission line analysis package developed by J. van der Merwe [3], and was used to perform the load variations for the experiment.

Simulations were performed on a Silicon Graphics IP28 195MHz workstation with 512MB of RAM.

#### 3.3.1 Frequency-Domain Code: NEC4D

NEC4D is a three-dimensional wire-based Method-of-Moments code. The transmission lines and terminations were created using Wiregrid, a NEC pre- and post-processor [4].

The Method-Of-Moments code is based on a combination of the definitions of the electric and magnetic potentials, equations (1.1) and (1.2), which for the case of a one-dimensional thin wire in free space reduce to the Pocklington Equation:

$$E(r) = \frac{1}{j\omega\epsilon_0} \int_{-l/2}^{l/2} \left[ \frac{\partial^2 \varphi}{\partial z^2} + k^2 \varphi \right] \cdot I \cdot dl \quad (3.3)$$

where  $E$  is the electric field strength in free space as a function of radial distance from the wire segment, the length of the wire segment is  $l$ , the current in the wire is

$I$ ,  $k$  is the propagation constant,  $\varphi$  is the free space Green's function and the wire is  $z$  directed. The free space Green's function is

$$\varphi = \frac{e^{-jkR}}{4\pi R} \quad (3.4)$$

The lossy ground is taken into account using Sommerfeld integrals [5]. This can only be performed numerically, and great care has been taken in NEC4D to integrate them correctly.

The entire metal structure is divided into short wire segments, each of which is assigned a weighted basis function which represents the amount of current flowing on that segment. The electric field  $E$  must be zero on each of the segments as they are ideal conductors, and thus there are as many equations as there are currents. A matrix inversion can be used to find the weights of the currents, providing a solution to the simulation.

NEC4D is a double precision code that extends the thin-wire approximations of (3.3). This makes the results from NEC4D accurate and reliable. However, matrix inversion is slow, and must be carried out for each frequency point. For this reason the NEC4D simulations take much longer to run than the time-domain code (see Table 3.2).

It is important that each of the transmission line's wires is terminated correctly in the simulation model. Test runs were used in order to find the best way to load a wire in NEC4D. Driving a single wire with a matched voltage source on one end, and loading it with a matched load on the other, allows simple transmission line theory to be compared to simulations. The expected current in the load is

$$I_L = \frac{V_S}{2Z_L} e^{-j\frac{\omega}{c}l} \quad (3.5)$$

$V_S$  is the source voltage,  $Z_L$  is the matched load impedance and  $l$  is the length of the transmission line.

The characteristic impedance of a single round wire above an ideal ground can be calculated from the per-unit-length parameters using (1.57), (1.70) and (1.71)

$$Z_c = \frac{1}{2\pi} \ln\left(\frac{2h}{R}\right) \sqrt{\frac{\mu}{\epsilon}} \quad (3.6)$$

$Z_c$  is the characteristic impedance,  $h$  is the height of the round wire above the ground plane and  $R$  is the radius of the round wire, as shown in Fig. 1.3. For the geometry used in the radiation robustness experiment (Table 3.1.), the characteristic impedance is approximately  $255 \Omega$ .

Various geometries were used to find a well modelled load in NEC4D. The wire was divided into 255 segments, each of which was thus 7.8 mm long. The largest possible phase error that this segmentation should produce is at 2 GHz, where 7.8 mm corresponds to  $18.8^\circ$ . The best method of loading the wires gave a magnitude error of 2.5% and a phase error of  $2.71^\circ$  at 1 GHz. Fig. 3.2 shows the loading used – vertical plates, with the segment connecting the plate to the transmission line loaded to the desired value.

### 3.3.2 Time-Domain Code: MTL\_SIM

The finite-difference time-domain (FDTD) code is MTL\_SIM [1], a one-dimensional code which steps through the scattered voltage formulation of the Telegrapher's equations (1.80) and (1.81), presented in Chapter 1 and repeated here in matrix form for multiple wires:

$$\frac{d\mathbf{V}^{\text{scat}}}{dz} + \mathbf{L}_\ell \frac{d\mathbf{I}}{dt} = \mathbf{V}_{s1} \quad (3.7)$$

$$\frac{d\mathbf{I}}{dz} + \mathbf{C}_\ell \frac{d\mathbf{V}^{\text{scat}}}{dt} = 0 \quad (3.8)$$

MTL\_SIM uses the matrix form of the Telegrapher's equations and approximates the derivatives with small increments:

$$\frac{1}{\Delta z} \begin{bmatrix} \mathbf{V}^{\text{scat}} \\ \mathbf{I} \end{bmatrix} + \frac{1}{\Delta t} \begin{bmatrix} \mathbf{0} & \mathbf{L}_\ell \\ \mathbf{C}_\ell & \mathbf{0} \end{bmatrix} \begin{bmatrix} \mathbf{V}^{\text{scat}} \\ \mathbf{I} \end{bmatrix} = \begin{bmatrix} \mathbf{V}_s \\ \mathbf{0} \end{bmatrix} \quad (3.9)$$

$\mathbf{V}_s$  a driving voltage source on the line, which for the radiation robustness experiment is set to zero. In equation (3.9) the per-unit-length parameters  $\mathbf{L}_\ell$  and  $\mathbf{C}_\ell$  are  $n \times n$  matrices as defined by (1.73) to (1.78).



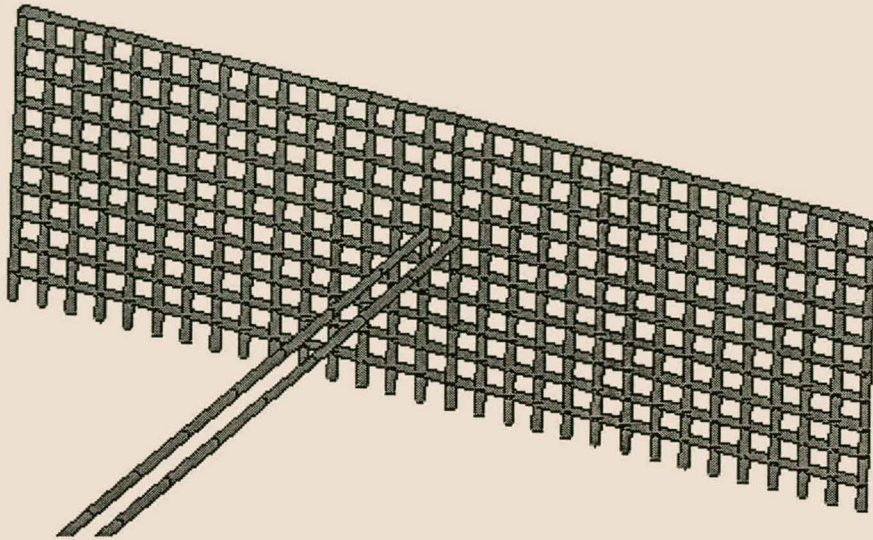


**Fig. 3.2. Wiregrid Diagram showing a Transmission Line Termination**

A utility program `L_theor`, which implements the equations, was written in MATLAB by J. van der Merwe. This program finds the mutual inductance matrix. There is no dielectric sheath around the wires, so the per-unit-length capacitance can be found from the equations (1.52) and (1.58).

The transmission line wires are divided into segments, and each segment is a unit cell as shown in Fig. 1.2 The scattered voltage vector  $\mathbf{V}^{\text{scat}}$  is found by numerically integrating the vertical scattered electric field between the ground and the wires. Thus the scattered voltage is found for each unit cell of the transmission line for every time step of the simulation, leading to large files for long simulations.

The program `FLD_CAL`, written by J. van der Merwe, is used to calculate the field strengths at each point along the line, for every time step. The source is assumed to be a plane wave, and the incident angles and polarisation of this wave are given to `FLD_CAL`, as well as a file describing the magnitude of the electric field strength of the wave for each time step. `FLD_CAL` performs a fast Fourier transform (FFT) on the input pulse and uses Fresnel reflection coefficients, based on (1.46) and (1.47) to calculate the electric field distributions. The vertical scattered electric field is numerically integrated to find the scattered voltage source for each unit cell. An inverse FFT is then used to convert the frequency information back into the time domain.

Transmission-line loads are described in MTL\_SIM by a state variable system, which allows non-linear loading. However, the frequency-domain code cannot handle non-linear loading, so only resistive terminations were used for purposes of comparison. The state variable system requires that there is a direct current path to ground. This is the case in the radiation robustness experiment.

The lossy ground is characterised by a two-pole approximation. The utility program GNDADIMP, also written by J. van der Merwe in MATLAB, allows the user to choose the pole positions. The permittivity and conductivity of the ground are described in terms of impedance and admittance, with high frequency asymptotic approximations.

The segmentation of the transmission line requires that the length of the segments be smaller than a fifteenth of a wavelength for accurate simulations:

$$\Delta x < \frac{\lambda_{\min}}{15} \quad (3.10)$$

The shortest wavelength is approximately 150 mm at 2 GHz, which leaves  $\Delta x < 10$  mm. For the sake of direct comparison the number of segments was chosen to be 255, which is identical to the NEC4D simulations, setting  $\Delta x = 7.8$  mm.

For a finite-difference time-domain code an additional requirement for the time increment is

$$\Delta t < \frac{\Delta x}{c} \quad (3.11)$$

which is a consequence of the maximum wave speed  $c$ . In this case the time step is set to  $\Delta t = 25$  ps. As the time step is the inverse of the sampling frequency of the input pulse, this sets the sampling frequency  $F_s$  to 40 GHz. This high sampling frequency means that there must be a large number of harmonically related frequencies across the 40 GHz band in order to have enough frequency points in the band of interest. This is an equivalent requirement to having a large number of time steps in the simulation. The maximum number of time steps that are handled reliably by MTL\_SIM is 8192, and this number was used in the radiation robustness experiment. It results in having 307 frequency points in the band 500 MHz to 2 GHz.



The total number of time steps and the length of each step give the total time simulated as 204.8 ns. As a wave travels up to the speed of light in free space, the time taken for a wave to travel once down the 2 m long transmission line is 6.67 ns. Thus the total simulation allows waves to travel 30 times back and forth along the lines. This should allow most of the signal to be dissipated in the loads, which results in accurate total power levels for the simulation.

An input pulse was synthesised using MATLAB to cover the 500 MHz to 2 GHz frequency range using 1024 harmonics. The inverse FFT function was applied to a vector of frequency points to create the pulse (see Appendix A). The pulse is centred on time zero as the harmonics in the pulse were given zero phase. In order to create the input file for FLD\_CAL the pulse was time-shifted to start after time zero, and zero padded to have 8192 points. In the frequency domain the shift creates a linear phase change for the harmonics and the zero padding increases the frequency resolution by adding more frequency points. The high sampling frequency is well above the Nyquist criterion of double the highest frequency of interest, and so aliasing is avoided. However, the time-domain signal is rectangle windowed when the simulation finishes. This creates ripple and sidelobes in the frequency domain.

Table 3.2 compares simulation times for the lossy ground, which were longer than for the ideal ground cases:

**Table 3.2 Comparison of Simulation Requirements for Ideal Ground Simulations**

	<b>CPU Time</b>	<b>Memory Requirement</b>	<b>Largest File Size</b>
<b>NEC4D</b>	1.76 min/frequency	81.9 MB	8.3 MB
<b>MTL_SIM</b>	15min / 307 frequencies	36.86 MB	35.5 MB

## 3.4 Measurement Setup

The physical measurement setup used an antenna as the noise source and an automatic network analyser (ANA) to make the measurements (in the frequency domain). The loads were constructed on microstrip to avoid capacitive and inductive effects as described in §3.4.3.

### 3.4.1 Antenna Placement

In order to approximate a uniform plane wave the antenna had to be placed far enough from the transmission lines so that the radial and azimuthal dependencies of the wave front at the transmission line wires were insignificant. In order to keep the amplitude of the wave front uniform, the wires were placed inside the 3 dB beamwidth of the main lobe of the antenna. In order to keep the phase of the wave front uniform, the wires were placed so as to accommodate the Rayleigh criterion. The distances required by these restrictions forced the measurement to be made outdoors. Test simulations of the experiment were run in both the time and the frequency domains. These tests were used to check the viability of the measurement setups, until a satisfactory setup was found.

The Rayleigh criterion is

$$R > \frac{2D^2}{\lambda} \quad (3.12)$$

where  $R$  is the separation distance,  $D$  is the effective length of the object being illuminated and  $\lambda$  is the wavelength. Equation (3.12) is most demanding at 2 GHz, where the wavelength is shortest. It was found that to fit into the limited space available, and to avoid the need for amplification, the maximum separation was limited to 10m, which left the effective length of the wires as 0.866 m. Thus the wires needed to be rotated relative to the plane wave. Fig. 3.3 is a diagram of the experimental setup.

### 3.4.2 Equipment Used

The antenna is a log-periodic dipole antenna with a gain of approximately 5 dB and a return loss better than -10dB in the frequency band 500 MHz – 2 GHz [6]. A 12

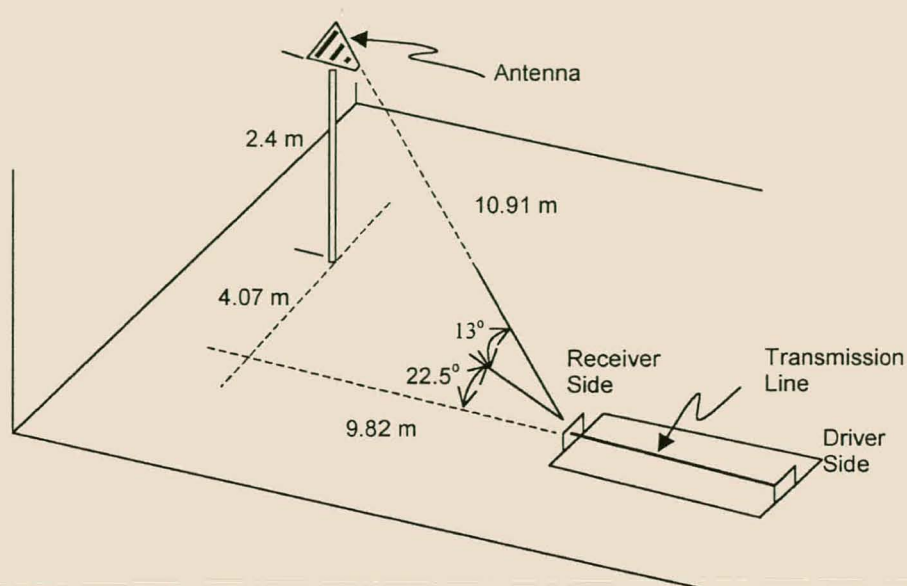


**Fig. 3.3. Diagram of Measurement Setup**

m length of Suhner RG214/U cable with a measured 3.5 dB return loss (for the entire length) at 1 GHz, connected the network analyser to the transmission line terminations, while several lengths of Suhner Sucoflex 104P (with 0.51 dB return loss per metre at 2 GHz) connects the antenna to the ANA. The ANA is an HP8753C calibrated in a 3.5 mm SMA medium.

The wires are stretched between two vertical plates above sections of allodyned aluminium for the ideal ground and a block of artificial absorber for the lossy ground. The artificial absorber was characterised in a Chapter 2 and found to have a conductivity of 0.04 S/m and a relative permittivity of 1.7. The terminations of the wires were created using chip resistors and microstrip in order to avoid stray capacitance and inductance. The microstrip circuit is shown in Fig. 3.4.

### 3.4.3 Transmission Line Terminations

Great care needs to be taken to avoid inductive or capacitive loading on the wires. At the same time some of the power must be transported to the ANA to make a measurement. The loading also had to take into account the fixed  $50\ \Omega$  medium of the ANA.

The ANA is connected through a plate (via a  $50\ \Omega$  SMA connector) to a short length of  $50\ \Omega$  microstrip transmission line. This means that (after the ANA is calibrated)

an ideal  $50\ \Omega$  load is present at the end of the microstrip line. The wires of the transmission line are attached near this end of the microstrip line. For a load less than  $50\ \Omega$ , a chip resistor is used to connect the transmission line to ground, while shimstock cut to the same width as the microstrip line connects the transmission line to the microstrip, creating a parallel resistance. For a load greater than  $50\ \Omega$  a chip resistor connects the transmission line to the microstrip, creating a series resistance. SMA connectors that are not attached to the ANA are loaded by  $50\ \Omega$  SMA terminations. The microstrip was built on a Taconic substrate with a height of 1.135 mm and a 2.48 dielectric constant, and LineCalc [7] was used to find the width of the line.

The microstrip circuits introduce power dividers that must be taken into account in order to establish the power dissipated in the total termination load. For the low impedance ( $25\ \Omega$ ) the power received in the termination is shared equally by a  $50\ \Omega$  chip resistor and the  $50\ \Omega$  ANA. Thus the measured power at the ANA must be doubled to find the power in the total load. For the matched impedance the power measured in the ANA is a 5 times smaller than the total power, and for the high impedance it is 50 times smaller.

### 3.4.4 Power Requirements for the Measurement

The power level of the source of the ANA is set to be as high as possible while

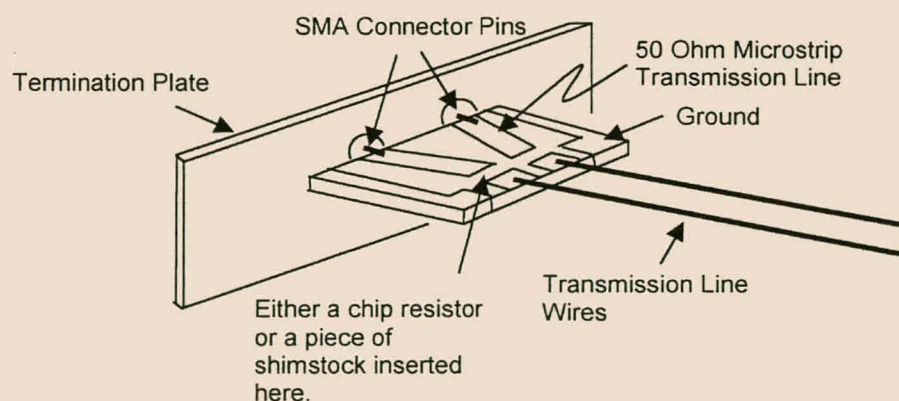


Fig. 3.4. Microstrip Termination Circuits

maintaining a high quality calibration. The source at port 1 was thus set to 15 dBm. It is necessary to find the signal-to-noise ratio (SNR) to ensure that a large enough signal reaches the ANA port 2 to make a good measurement.

The signal at the source is 15 dBm. The Suhner Sucoflex cables introduce at most 2dB loss, which reduces the signal to 13 dBm. The electric field strength can be found from

$$\bar{S} = \frac{W_{IN} G}{4\pi r^2} \quad (3.13)$$

$$\bar{S} = \frac{E_{peak}^2}{2\eta_0} \quad (3.14)$$

where  $\bar{S}$  is the root-mean-square (RMS) power in the plane wave. For the antenna with gain 5 dB, the peak electric field will be approximately 0.22 V/m. From simulations a plane wave with electric field 0.22 V/m delivers approximately -50 dBm to -80 dBm into a termination. This termination (for a low impedance) is a part of a power divider that delivers half of the power to the ANA leaving approximately -83 dBm. There is a 12 m stretch of Suhner RG214/U which introduces an estimated 8 dB loss at 2 GHz, which further reduces the signal power to -90 dBm. This is still above the noise floor of the ANA, which is at approximately -100 dBm with the IF bandwidth set to 10 Hz. Thus the measurement power levels are adequate without the use of an amplifier.

### 3.4.5 Power Normalisation for Comparison

In order to compare the simulations and measurements it is necessary to normalise the received power by the power in the incident wave. For the simulations, equation (3.14) can be used to find the average power in the incident wave. NEC4D runs a single frequency point at a time with an incident wave peak electric field of 1 V/m, while the MTL\_SIM peak electric field is not fixed at 1 V/m because of windowing introducing ripple. For the measurement  $S_{21}$  can be used to relate the measured power to the power in the incident field by removing the gain of the antenna and the  $\frac{1}{r^2}$  free space travel from the measurement.



### 3.4.6 Loading Variations

The loads were chosen relative to the transmission line's characteristic impedance. In this case  $L_{\text{theor}}$  predicts the characteristic impedance to be approximately  $255\ \Omega$ . Thus a "low" impedance is approximately a tenth or  $25\ \Omega$ , while a "high" impedance is approximately ten times greater or  $2500\ \Omega$ . To further simplify the problem all the wires were terminated with the same impedance on any one side.

The loads are varied as shown in Table 3.3. The amount of noise current on the wire closest to the incident wave on the receiver side is used to find the noise power in the system. The "receiver" and "driver" loads referred to in Table 3.3 are the ends of the transmission line as shown in Fig 3.3.

**Table 3.3. Loading Variations Used in Radiation Robustness Experiment**

Measurement	Receiver Load	Driver Load
1	Low	Low
2	Low	Matched
3	Low	High
4	Matched	Low
5	Matched	Matched
6	Matched	High
7	High	Low
8	High	Matched
9	High	High

## 3.5 Wires Above a Perfectly Electrically Conducting Ground

MTL\_SIM and NEC4D are compared to a measurement over an ideal ground in Fig. 3.5 and Fig. 3.6 respectively.

The noise power levels are  $-30\ \text{dB}$  to  $-70\ \text{dB}$  below the power in the incident wave. If the incident wave were to contain  $1\ \text{W}$  incident from  $10\ \text{m}$  away, perhaps from a cellular telephone, between  $1\ \mu\text{W}$  and  $1\ \text{pW}$  of noise power would be received in the low load. This may well be enough to interfere with a sensitive system.

The graphs show a ringing across the band with a frequency of approximately 70 MHz, which corresponds to the travel time of waves along the 2 m long wires. The null at approximately 1.3 GHz was found to be sensitive to within a fraction of a degree of angle of plane wave incidence, a requirement that cannot be met by the tolerances of the measurement. This explains the several hundred MHz difference between the frequencies of the measured and simulated nulls.

In Fig. 3.7, 3.8 and 3.9 the MTL\_SIM simulations are used to compare the effects of varying the termination loads.

The different loading shifts the peaks and nulls of the ringing. This is because changing a load from high to low, or vice versa, involves a sign change of the reflection coefficient. Thus the interference patterns change and the peaks and nulls move.

When neither end is matched the ringing is approximately 15 dB. When one end is matched the ringing drops to 2 to 5 dB, while the minimum power level drops by approximately 10 dB. The least power is received into the low impedance of the Low – Matched pair. The maximum power difference between configurations is almost 30 dB, indicated the effectiveness of loading.

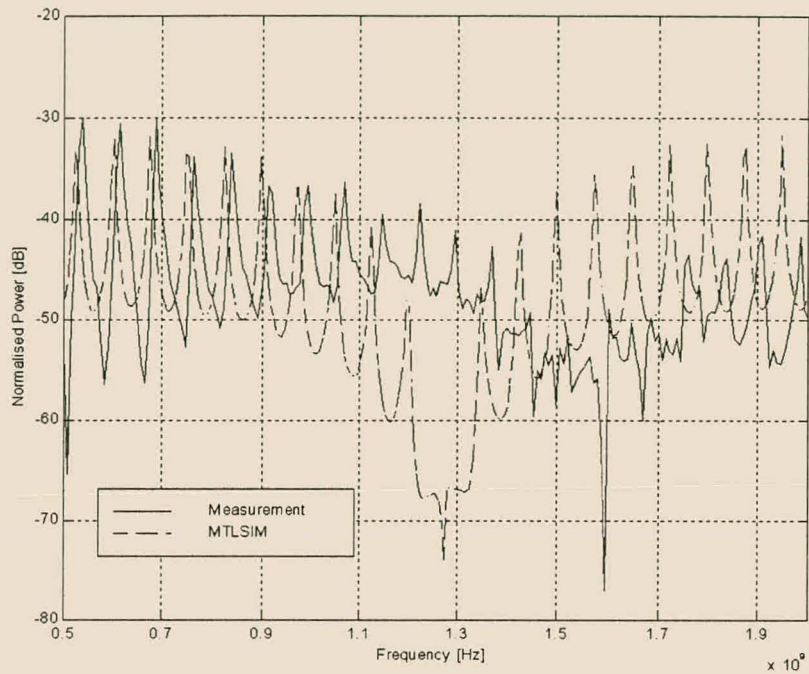


**Fig. 3.5. Comparison of Measurement and MTL\_SIM for Low – Low Loading Above an Ideal Ground**

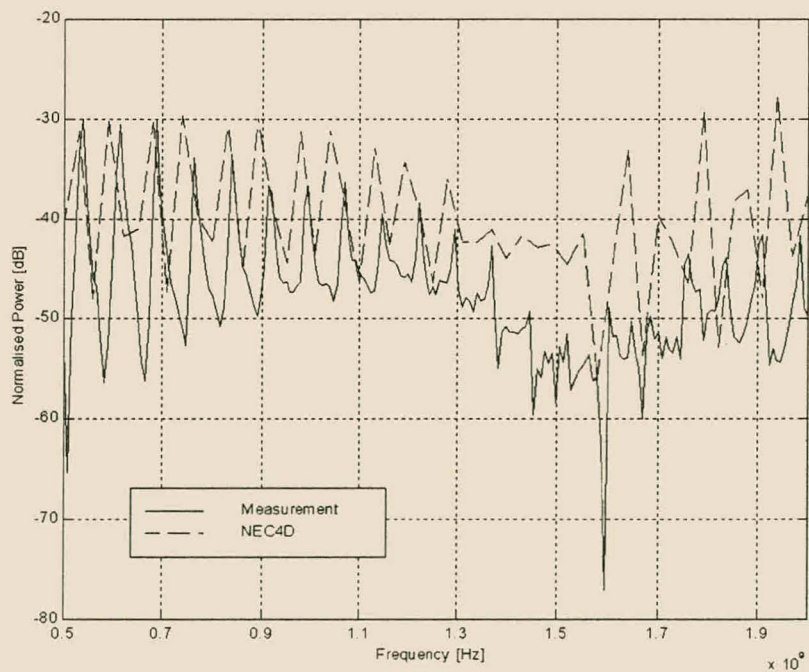


**Fig. 3.6. Comparison of Measurement and NEC4D for Low - Low Loading Above an Ideal Ground**



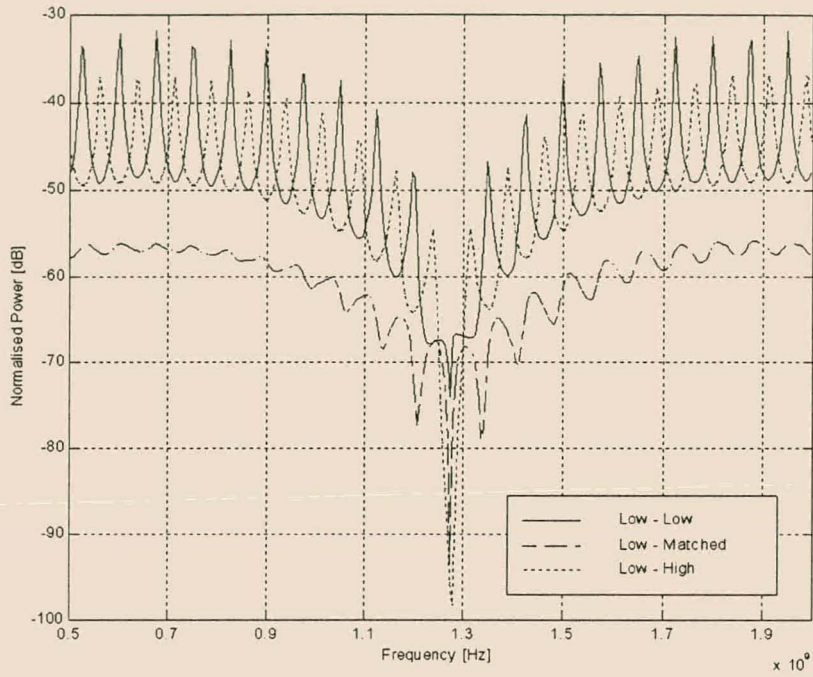


**Fig. 3.7. MTL\_SIM Comparison of Power Received in Low Load Above an Ideal Ground**

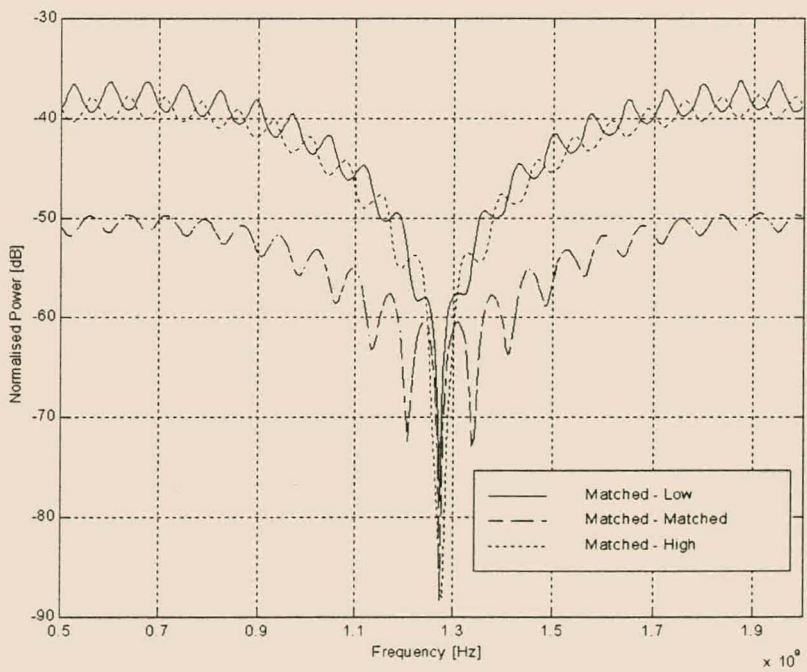


**Fig. 3.8. MTL\_SIM Comparison of Power Received in Matched Load Above an Ideal Ground**

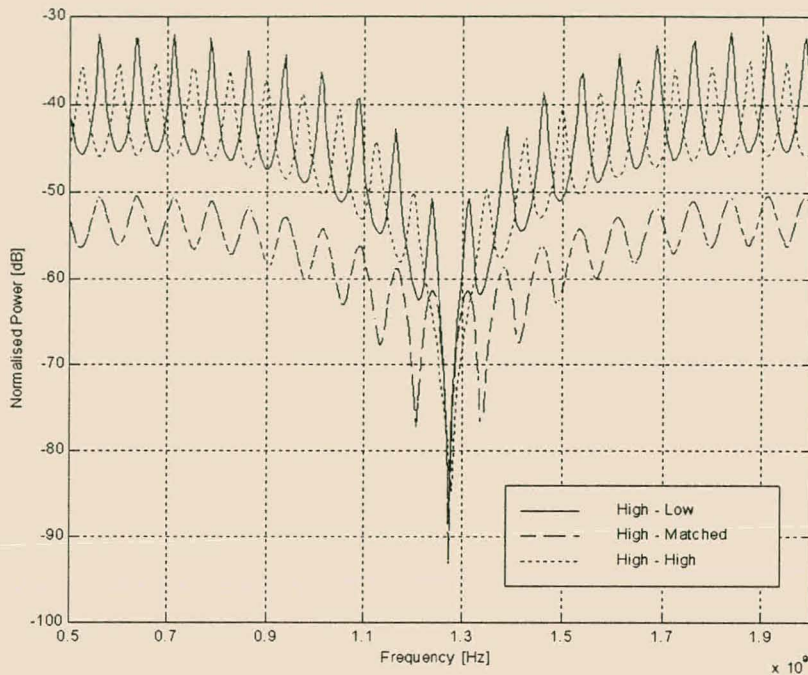


Fig. 3.9. MTL\_SIM Comparison of Power Received in High Load Above an Ideal Ground

### 3.6 Wires Above a Lossy Ground

The ideal ground is substituted by a dielectric block, with approximate dimensions  $2 \times 1 \times 0.3$  m. It is important that the terminations make good electrical contact with the dielectric block to prevent unexpected open circuits or lossy connections. For this reason two copper plates measuring  $1\text{m} \times 0.3\text{m}$  are clamped to the ends of the dielectric block. The microstrip termination circuits are connected to these vertical plates, ensuring good electrical contact.

Comparisons between a measurement and simulations are shown in Fig. 3.10 and 3.11. The transmission lines are loaded by a matched load on the receiver side and a high load on the driver side. Again there is agreement between the measurement and the MTL\_SIM simulation, although some nulls are replaced by peaks over the middle frequencies of the simulation, something not seen in the measurement. However, the NEC4D simulations compare poorly with the measurement. This is unexpected, as the NEC4D simulation is using the exact Sommerfeld integrals,

which should be more accurate than the Fresnel reflection coefficients used by MTL\_SIM. A series of simulations were run to investigate the cause of this behaviour. It was found that the NEC4D simulation differed from the MTL\_SIM simulations most widely when the vertical angle of incidence was low.

The lossy ground has attenuated the signal at the higher frequencies by approximately 5 dB, while the ringing has changed from the ideal ground case to have soft peaks and deep nulls. Fig. 3.12, 3.13 and 3.14 show the power received in the receiver load while the driver load is varied. Fig. 3.13 shows that unlike the ideal ground case, matching the load above a lossy ground increases the amount of power received. However, the lowest power received is still the Low – Matched case.

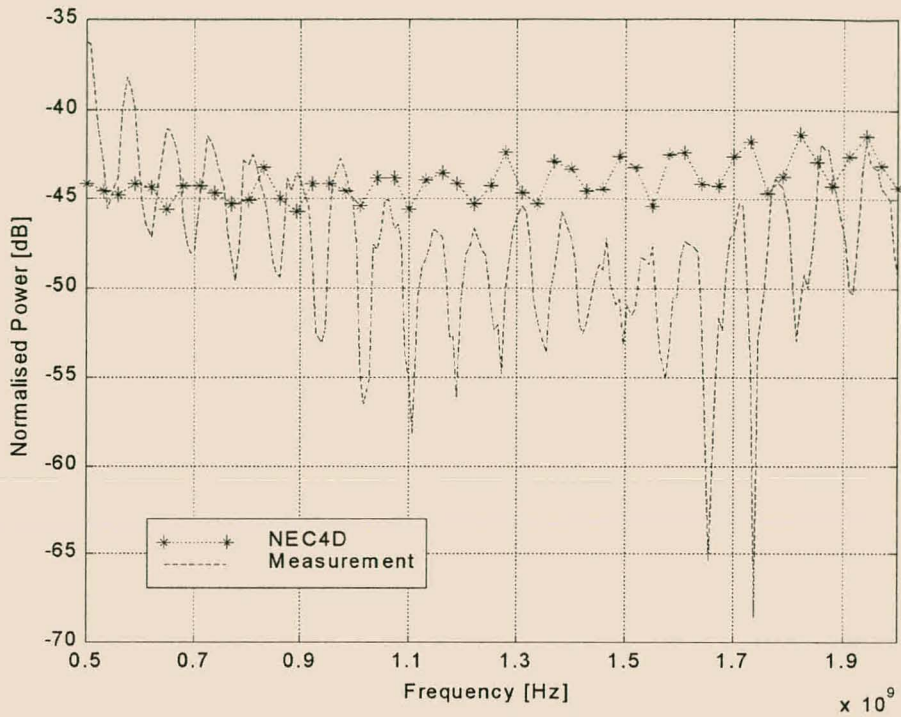


**Fig. 3.10. Comparison of Measurement and NEC4D for Matched – High Loading above Lossy Ground**

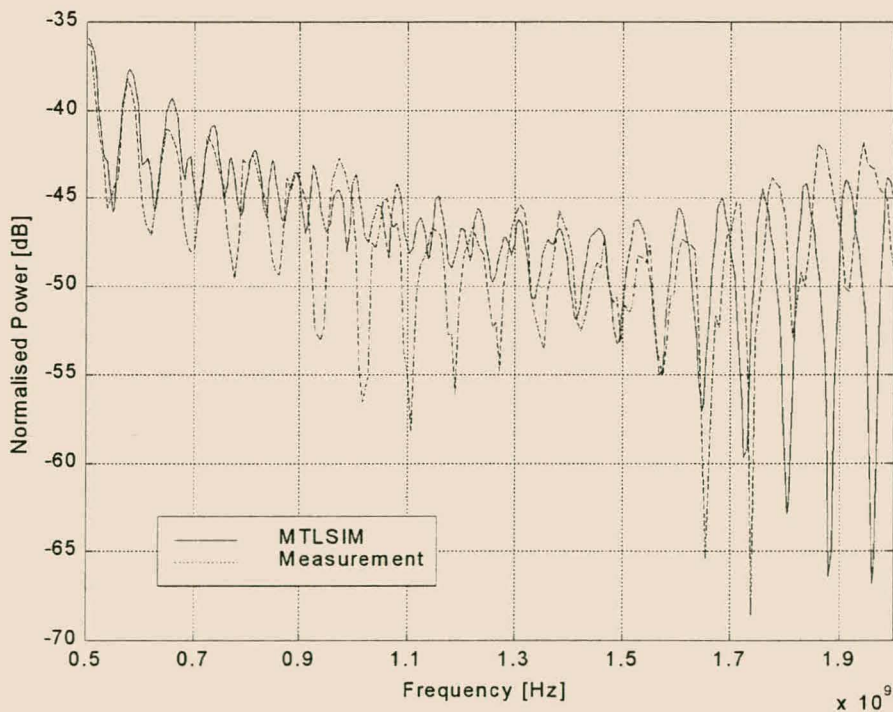


**Fig. 3.11. Comparison of Measurement and MTL\_SIM for Matched – High Loading above Lossy Ground**



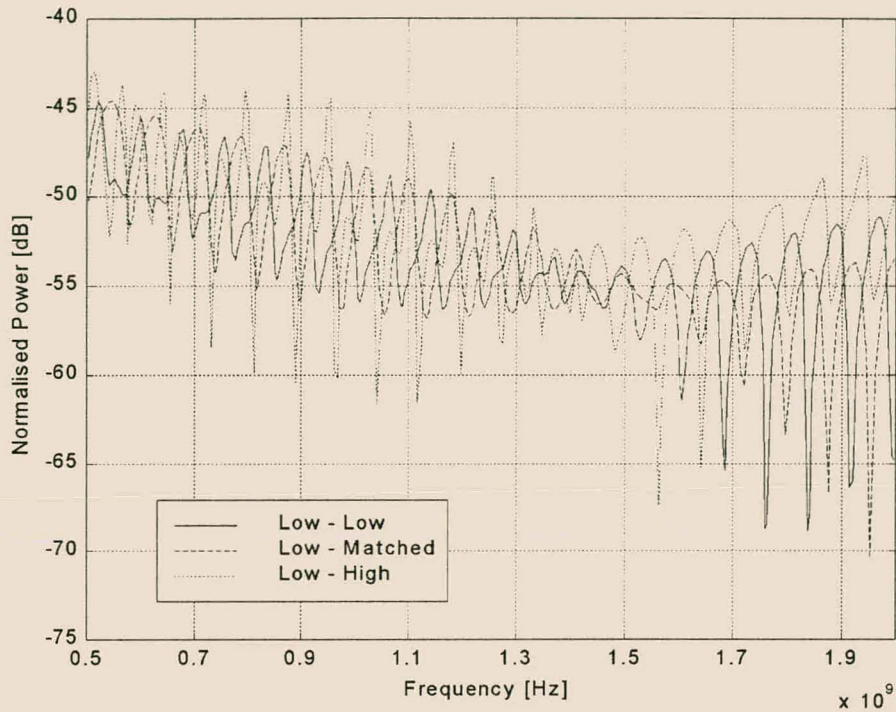


**Fig. 3.12. MTL\_SIM Comparison of Power Received in a Low Load for Wires Above a Lossy Ground**

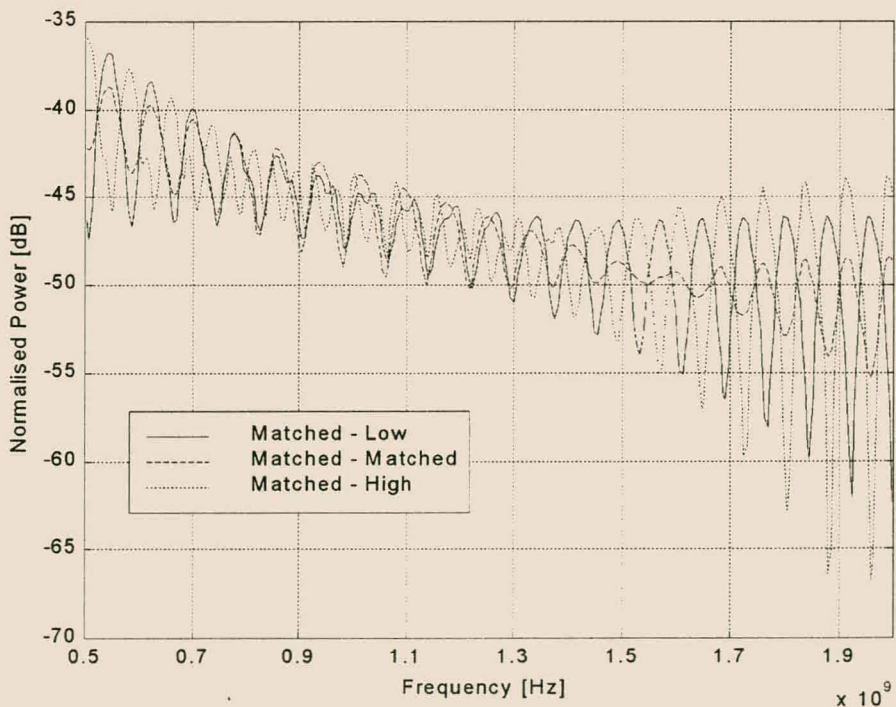


**Fig. 3.13. MTL\_SIM Comparison of Power Received in a Matched Load for Wires Above a Lossy Ground**

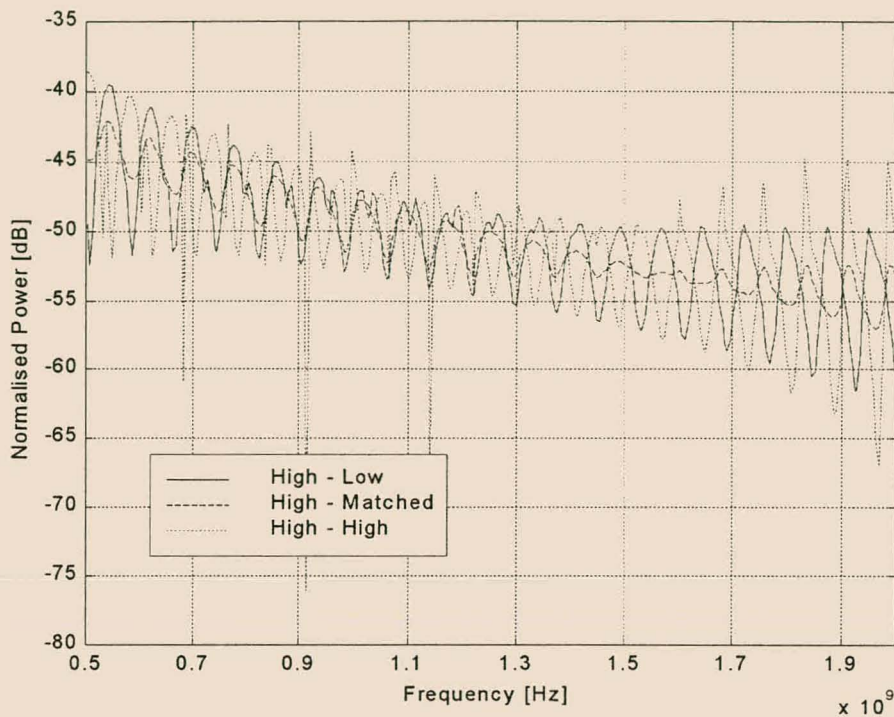


**Fig. 3.14. MTL\_SIM Comparison of Power Received in a High Load for Wires Above a Lossy Ground**

### 3.7 Conclusion

The radiation robustness experiment required the ability to accurately simulate the effect that variations of the load on the transmission line have. The time-domain simulation package MTL\_SIM proved to be accurate and fast. In order to confirm the accuracy of the simulations it was necessary to make measurements of the system. The measurements corresponded well to MTL\_SIM above both an ideal and a lossy ground, proving the value of both pieces of work.

NEC4D was used as a standard with which to compare MTL\_SIM. NEC4D proved to be both slower and less accurate, especially above a lossy ground. This was unexpected.

The radiation robustness experiment was carried out over both an ideal and a lossy ground. Interestingly, the highest power levels were seen when the wires were over the lossy ground, and not, as might be expected, above the ideal ground. This was



seen by [4, §8.5.1] and confirmed here. The effect occurs because tangential E-fields can excite currents in the lossy ground, but not on the ideal ground.

The close match between the measurements and MTL\_SIM simulations above the lossy ground also confirm that the material property measurements discussed in Chapter 2 were accurate enough for the two-pole approximation used by MTL\_SIM.

It is clear that system robustness is heavily influenced by the transmission line loading, where power levels can be reduced by up to approximately 15 dB. This is where there is a Low termination on one end and a High termination on the other. Using this simple rule-of-thumb and knowledge of a transmission line's characteristic impedance can thus reduce the risk of system failure at minimal cost.

Note that this rule-of-thumb does not take the signal power levels and device characteristics into account. These complications are important but are not dealt with here as they are different for every system. What the work in this chapter has demonstrated is the ability to measure and simulate this kind of system accurately. Using the time-domain simulation package a system designer can find the noise power levels in a system and deal with them appropriately.

### 3.8 References

- [1] J. van der Merwe, *Multiconductor Lines Above Dissipative Earth: Direct FDTD Analysis and Experimental Validation*, Ph.D. Dissertation, University of Stellenbosch, October 1998.
- [2] G. J. Burke, *Numerical Electromagnetics Code – NEC-4 Method of Moments Part I: User's Manual (NEC-4.1)*, Lawrence Livermore National Laboratory, January 1992.
- [3] J. van der Merwe, *Users Guide for MTL\_Sim*, Department of Electrical and Electronic Engineering, September 1998.
- [4] F. M. Tesche, M. V. Ianoz and T. Karlsson, *EMC Analysis Methods and Computational Models*, John Wiley & Sons, 1997.
- [5] C. A. Balanis, *Advanced Engineering Electromagnetics*, John Wiley & Sons, 1989.
- [6] M. J. van Wyk, *Development of a Three-Octave Bandwidth Printed Log-Periodic Dipole Array*, M.Sc. Thesis, University of Stellenbosch, 1998.

- [7] Touchstone & Libra for Windows, Eesof Incorporated, Lindero Canyon Road, Westlake Village, CA, February 1993.

## CONCLUSION

---

This thesis looked at an aspect of EMC that up until recently was a focus only for nuclear electromagnetic pulse research. As electronics develops, traditional borders between low and high frequencies and digital and analogue electronics are blurring. It is important for designers to take into account much wider spectrums and different sources of power as the density of electrical systems increases.

The origin of the specific study, radiation to transmission lines with variable loading, comes directly from the open-bed mining industry. Industry focus remains an important part of EMC research. However, the results from the thesis are far more widely applicable, as the ability to measure and simulate wire systems paves the way for investigations into a wide set of problems ranging from power distribution to communications.

During the thesis a good theoretical understanding of the field distributions was developed and the unique features of transverse electromagnetic waves were employed. More complicated wave distributions caused by the lossy ground were handled as a perturbation to the original TEM solution. As is often the case with electromagnetic systems, the analytical solution is unable to handle the complete system but instead forms the basis for numerical techniques.

Successful simulations were performed in the time and frequency domains. The frequency domain code was used as a standard with which to compare the time-domain transmission line code. For the purposes of comparison between the codes, only resistive loading was used, but the ability of the time domain code to handle time-dependent loads would be an obvious advantage, especially when switching systems are to be examined.

The good agreement between the simulations and measurement also demonstrates the ability of the EMC researcher to measure less easily defined systems. The

measurements demonstrate that the transmission line approximations made by the time-domain code are valid. Thus the simulations can be used as a first step toward accurate synthesis of transmission line systems. This is a great advantage in a field where most synthesis is performed using rules of thumb.

The results from the comparisons between the power received at the transmission line terminations shows that a designer can create a far more robust system for the minimal costs of greater power loss in the resistors, and expensive options such as shielding can be avoided. The results of this thesis thus provide a solution directly applicable to industry, which is always interested in cost effective options.

A broad argument is made that the minimisation of externally excited noise power in a wiring system is desirable. In general terms this argument is a good starting point. However, covering all aspects of radiation robustness would require investigations into the effects of signal-to-noise ratios, out-of-band noise, edge-triggered events and non-linear terminations. It is also important to take into account situations where the low noise power creates a high voltage over a voltage sensitive device, or a high current into a current sensitive device. All these aspects would form a valuable future research program. This thesis presents and validates a technique to establish the noise power levels in a system – a system designer must also take the signal power levels and device characteristics into account.

# 1 MATLAB Routine to Solve for the Electric Field Potential

```

function CS = lapsol2(width,height,boundCond,errorPerc,check);

%function CS = lapsol2(width,height,boundCond,errorPerc,check);
%
%Numerically solves Laplace's equation for a bounded source free region.
%
% boundCond is a matrix containing the boundary conditions, errorPerc is
% the tolerance of the largest difference between successive runs, check is
% a boolean to plot the boundary conditions.
%
%Written by Thomas Stuart 30-03-1998

%Dimensions
w = width;
h = height;

disp('Matrix dimensions:')
w
h

disp('Convergence to ');
disp(errorPerc)
disp('=====')

%CREATE CROSS-SECTION
global CS
CS = 0.5*ones(w,h);
bc = ones(w,h);
%CREATE BOUNDARY CONDITIONS
%Find the number of boundary conditions
numBound = size(boundCond,1); %Returns just the number of rows
for cond=1:numBound
    %Read the boundary condition matrix
    Xmin = boundCond(cond,1);
    Xmax = boundCond(cond,2);
    Ymin = boundCond(cond,3);
    Ymax = boundCond(cond,4);
    pot = boundCond(cond,5);

    %Insert boundary conditions
    for xInc = Xmin:Xmax
        for yInc = Ymin:Ymax
            %Insert the potential
            CS(xInc,yInc) = pot;
            %Fix the boundary conditions
            bc(xInc,yInc) = 0;
        end;
    end;
end;

end;

%DISPLAY BOUNDARY CONDITIONS IF DESIRED
if check
    mesh(CS);grid,axis('square');
    disp('Check conditions and press any key....')
    pause

```

```

end;

%FIND ELECTROSTATIC SOLUTION
%Convert error from percentage
error = errorPerc;
diff = error;
%Cycle until the largest difference is less than the error
while (diff>=error)
    maxDiff=0;
    %First calculate the points away from the rim
    for xInc=2:w-1
        for yInc=2:h-1
            %If the point is not a boundary condition
            if (bc(xInc,yInc)~=0)
                oldCS = CS(xInc,yInc);
                %then calculate average of the points around it
                CS(xInc,yInc)=( CS(xInc,yInc-1) + CS(xInc-1,yInc)+ CS(xInc,yInc+1) +
CS(xInc+1,yInc) )/4;
                newCS = CS(xInc,yInc);
                tempDiff = abs(newCS-oldCS);
                if (tempDiff>maxDiff)
                    maxDiff = tempDiff;
                end;
            end; %if
        end; %for
    end; %for
    disp(maxDiff);
    if (maxDiff<diff)
        diff=maxDiff;
    end;

    %Potentials at the edges
    %Potentials at the corners are made equal to the potentials just inside the corners
    if (bc(1,1)~=0) %is not a boundary condition
        CS(1,1) = CS(2,2);
    end;
    if (bc(1,h)~=0) %is not a boundary condition
        CS(1,h) = CS(2,h-1);
    end;
    if (bc(w,h)~=0) %is not a boundary condition
        CS(w,h) = CS(w-1,h-1);
    end;
    if (bc(w,1)~=0) %is not a boundary condition
        CS(w,1) = CS(w-1,2);
    end;

    %Now the four edges
    for xInc=2:w-1
        if (bc(xInc,1)~=0) %is not a boundary condition
            CS(xInc,1) = CS(xInc,2);
        end;
    end;
    for xInc=2:w-1
        if (bc(xInc,h)~=0) %is not a boundary condition
            CS(xInc,h) = CS(xInc,h-1);
        end;
    end;
    for yInc=2:h-1
        if (bc(1,yInc)~=0) %is not a boundary condition
            CS(1,yInc) = CS(2,yInc);
        end;
    end;
    for yInc=2:h-1
        if (bc(w,yInc)~=0) %is not a boundary condition
            CS(w,yInc) = CS(w-1,yInc);
        end;
    end;
end; %while

```



## 2 MATLAB Routine to Synthesize a Pulse

```

function [pulse,delt] = makepulse(Fs,Fmin,Fmax,N);

%function [pulse,delt] = makepulse(Fs,Fmin,Fmax,N);
%
% Creates a pulse with specific frequency components for MTL_sim.
%
% Fs is the sampling frequency, 1/delt; N is the number of (harmonically
% related) frequency points across the entire spectrum.

%Written by Thomas Stuart
%November 1998

%CREATE THE AMPLITUDE ARRAY
%Initialise array
X = zeros(1,N);

%Find the harmonic interval
fspace = Fs/(N-1);

%Fill the array with signals amplitude 1 phase 0
%Include both positive and negative frequencies making sure to include the desired band
for n=1:N
    X(n) = ( ((fspace*(n-1))>(Fmin-fspace))&((fspace*(n-1))<Fmax+fspace) ) | (
    ((fspace*(n-1))>(Fs-(Fmax+fspace)))&((fspace*(n-1))<(Fs-(Fmin-fspace))) );
end;

%Plot the frequency domain signal
frange = linspace(0,Fs,N);
figure;
plot(frange,X,'-x');grid on;
xlabel('Frequency [Hz]');
ylabel('Amplitude');
pointsInBand = sum((X==1))/2;
title(['Frequency Range of Pulse (No points in band = ',num2str(pointsInBand),')']);

%Find the time domain pulse
x = ifft(X);
x = real(fftshift(x));

%Plot the time domain signal
figure;
trange = linspace(-N/2/Fs,N/2/Fs,N+1);
plot(trange,[x x(1)]);
xlabel('Time [s]');
ylabel('Magnitude');
grid on;
title('Pulse in the Time Domain');

%Create the output parameters
pulse = x;
delt = 1/Fs;

```